

This is an Open Access document downloaded from ORCA, Cardiff University's institutional repository: <https://orca.cardiff.ac.uk/id/eprint/118875/>

This is the author's version of a work that was submitted to / accepted for publication.

Citation for final published version:

Faruqu, Farid N., Tzu-Wen Wang, Julie, Xu, Lizhou, McNickle, Luke, Ming-Yiu Chong, Eden, Walters, Adam, Gurney, Mark, Clayton, Aled, Smyth, Lesley A., Hider, Robert, Sosabowski, Jane and Al-Jamal, Khuloud T. 2019. Membrane radiolabelling of exosomes for comparative biodistribution analysis in immunocompetent and immunodeficient mice – a novel and universal approach. *Theranostics* 9 (6), pp. 1666-1682. 10.7150/thno.27891

Publishers page: <http://dx.doi.org/10.7150/thno.27891>

Please note:

Changes made as a result of publishing processes such as copy-editing, formatting and page numbers may not be reflected in this version. For the definitive version of this publication, please refer to the published source. You are advised to consult the publisher's version if you wish to cite this paper.

This version is being made available in accordance with publisher policies. See <http://orca.cf.ac.uk/policies.html> for usage policies. Copyright and moral rights for publications made available in ORCA are retained by the copyright holders.



# Membrane radiolabelling of exosomes for comparative biodistribution analysis in immunocompetent and immunodeficient mice – a novel and universal approach

Farid N. Faruqu<sup>1</sup>, Julie Tzu-Wen Wang<sup>1</sup>, Lizhou Xu<sup>1</sup>, Luke McNickle<sup>1</sup>, Eden Ming-Yiu Chong<sup>1</sup>, Adam Walters<sup>1</sup>, Mark Gurney<sup>2</sup>, Aled Clayton<sup>2</sup>, Lesley A. Smyth<sup>3</sup>, Robert Hider<sup>1</sup>, Jane Sosabowski<sup>4\*</sup>, Khuloud T. Al-Jamal<sup>1\*</sup>

<sup>1</sup> Institute of Pharmaceutical Science, Faculty of Life Sciences & Medicine, King's College London, Franklin-Wilkins Building, 150 Stamford Street, London SE1 9NH, United Kingdom

<sup>2</sup> School of Medicine, Tenovus Building, University Hospital of Wales, Heath Park, Cardiff, CF14 4XN

<sup>3</sup> School of Health Sport and Bioscience, University of East London, Water Lane, London E15 4LZ

<sup>4</sup> Centre for Molecular Oncology, Barts Cancer Institute, Queen Mary University of London, Charterhouse Square, London EC1M 6BQ

\*Corresponding authors:

Prof. Khuloud T. Al-Jamal

Email address: khuloud.al-jamal@kcl.ac.uk (K.T. Al-Jamal).

Dr. Jane Sosabowski

Email address: j.k.sosabowski@qmul.ac.uk (J.K. Sosabowski).

## Abstract

Extracellular vesicles, in particular exosomes, have recently gained interest as novel drug delivery vectors due to their biological origin and inherent intercellular biomolecule delivery capability. An in-depth knowledge of their *in vivo* biodistribution is therefore essential. This work aimed to develop a novel, reliable and universal method to radiolabel exosomes to study their *in vivo* biodistribution.

**Methods:** Melanoma (B16F10) cells were cultured in bioreactor flasks to increase exosome yield. B16F10-derived exosomes (EXO<sub>B16</sub>) were isolated using ultracentrifugation onto a single sucrose cushion, and were characterised for size, yield, purity, exosomal markers and morphology using Nanoparticle Tracking Analysis (NTA), protein measurements, flow cytometry and electron microscopy. EXO<sub>B16</sub> were radiolabelled using 2 different approaches – intraluminal labelling (entrapment of <sup>111</sup>Indium *via* tropolone shuttling); and membrane labelling (chelation of <sup>111</sup>Indium *via* covalently attached bifunctional chelator DTPA-anhydride). Labelling efficiency and stability was assessed using gel filtration and thin layer chromatography. Melanoma-bearing immunocompetent (C57BL/6) and immunodeficient (NSG) mice were injected intravenously with radiolabelled EXO<sub>B16</sub> (1x10<sup>11</sup> particles/mouse) followed by metabolic cages study, whole body SPECT-CT imaging and *ex vivo* gamma counting at 1, 4 and 24 h post-injection.

**Results:** Membrane-labelled EXO<sub>B16</sub> showed superior radiolabelling efficiency and radiochemical stability (19.2 ± 4.53 % and 80.4 ± 1.6 % respectively) compared to the intraluminal-labelled exosomes (4.73 ± 0.39 % and 14.21 ± 2.76 % respectively). Using the membrane-labelling approach, the *in vivo* biodistribution of EXO<sub>B16</sub> in melanoma-bearing C57BL/6 mice was carried out, and was found to accumulate primarily in the liver and spleen (~56% and ~38% ID/gT respectively), followed by the kidneys (~3% ID/gT). EXO<sub>B16</sub> showed minimal tumour i.e. self-tissue accumulation (~0.7% ID/gT). The membrane-labelling approach was also used to study EXO<sub>B16</sub> biodistribution in melanoma-bearing immunocompromised (NSG) mice, to compare with that in the immunocompetent

C57Bl/6 mice. Similar biodistribution profile was observed in both C57BL/6 and NSG mice, where prominent accumulation was seen in liver and spleen, apart from the significantly lower tumour accumulation observed in the NSG mice (~0.3% ID/gT).

**Conclusion:** Membrane radiolabelling of exosomes is a reliable approach that allows for accurate live imaging and quantitative biodistribution studies to be performed on potentially all exosome types without engineering parent cells.

**Key words:** Exosomes, drug delivery, radiolabelling, biodistribution

## Introduction

Exosomes are a subtype of extracellular vesicles (EV) ranging from 50-200 nm in diameter, secreted by various cell types such as dendritic cells [1], macrophages [2], cancer cells [3-6] and mesenchymal stem cells [7]. Exosomes have also been shown to be present in various physiological fluids [8-11]. The combination of the inherent ability of exosomes to carry various biomolecules (e.g. RNA and proteins) [12, 13] and the effective delivery of these biomolecules into recipient cells [14-16] attracted interest for their potential as nano-scale drug delivery vectors for a multitude of therapeutic agents. Small molecule-drugs such as doxorubicin [17-19], paclitaxel [20], imatinib [21], curcumin [22-24], acridine orange [25] and anthocyanidin [26] have been demonstrated to be successfully loaded into exosomes and delivered to target cells. Nucleic acids such as siRNA [27, 28] and microRNA [29] have also been successfully loaded into exosomes *via* electroporation and delivered to target cells. Exosomes can also be engineered for targeted delivery, mostly by means of expressing the targeting moiety as a fusion protein with transmembrane proteins on the exosomes [14]. The RVG peptide-Lamp2b fusion protein was the first to be demonstrated to target exosomes across the blood-brain barrier (BBB) for brain delivery [30]. Exosomes bearing the GE11 peptide-PDGFR fusion protein were shown to target EGFR-overexpressing breast cancer cell lines [31]. Interestingly, non-targeted exosomes have been reported to home to their tissue or cell of origin [32], suggesting that exosomes might have inherent targeting ability without requiring any engineering.

Given the huge interest and potential in developing exosomes as drug delivery vectors, it is essential to understand their *in vivo* biodistribution. Several studies have been conducted to analyse this, mostly involving labelling exosome with fluorescent probes to track them *in vivo via* qualitative live imaging or quantitative *ex vivo* organ analysis. The major drawback of this technique is auto-fluorescence and tissue penetration depth during live imaging, even when using near infrared (NIR) fluorescent probes, therefore requiring the animals to be culled and organs excised for *ex vivo* imaging for more reliable results [18, 31-33]. This makes optical imaging limited to end-point analysis and not amenable to longitudinal studies or those that involve multiple dosing on the same animal. *Ex vivo* organ analysis using this modality also harbours substantial inaccuracies, as the

fluorescence from the excised organs are detected in a 2D-manner. Combined with the limited tissue penetration depth of fluorescent probes, this results in partial loss of signals and therefore rendering the biodistribution analysis only semi-quantitative [18, 32, 33]. Labelling using lipophilic dyes such as PKH26 or DiR have been reported to suffer from non-specific transfer of the dye between membranes, which heavily and adversely influenced the accuracy of the results obtained in the studies carried out [34-36]. The long half-life of these lipophilic dyes adds to the drawback described above, where it is not possible to distinguish whether the signal is coming from the labelled body of interest or free dye transferred to another membrane. Therefore, the reliability and accuracy of organ biodistribution of exosomes labelled using such dyes is questionable.

Other modalities such as bioluminescence has also been explored, whereby the exosomes were engineered to express luciferase on their surface, effectively creating bioluminescent exosomes upon introduction of its substrate. This modality eliminates the problem of auto-fluorescence but requires genetic modification of the parent cells from which the exosomes originate. This can be challenging to perform on primary cells and is not possible for exosomes isolated from physiological fluids [37, 38].

Labelling the exosomes with radioactive isotopes for tracking them *in vivo* is a more robust modality for evaluating both qualitative and quantitative exosome biodistribution *via* live SPECT or PET imaging and *ex vivo* organ analysis, as it does not have the limitations associated with the modalities described above. However, only a limited number of studies have been carried out, and in these cases the radiolabelling techniques suffer from serious limitation. In one study, the exosomes were engineered to express streptavidin as a fusion protein on their membrane, and radiolabelling was achieved when incubated with <sup>125</sup>I-tagged biotin [39]. Again, this method requires genetic modification of the parent cells and is therefore not applicable to all types of exosomes. Another study carried out radiolabelling by entrapping the <sup>99m</sup>Tc-HMPAO complex within the lumen of exosome nanomimetics (cells extruded to become vesicles of similar size to exosomes), *via* an in-situ glutathione-dependent reduction of the HMPAO chelator [40]. The success of application of this method to actual exosomes is uncertain as glutathione, the key molecule for this radiolabelling method, is only found in very low amounts in exosomes [41]. A similar method of entrapping the radioisotope for labelling exosomes is used in a

different study, where the  $^{111}\text{In}$ -oxine complex was used to shuttle the  $^{111}\text{In}^{3+}$  ions inside the exosomal lumen [18]. Oxine however, has been discontinued as a commercially available radiolabelling kit.

In this study, two novel exosome radiolabelling approaches using  $^{111}\text{In}^{3+}$  as the radioisotope were explored. One method involves radioisotope entrapment approach similar to oxine, but using tropolone, a safe and cheap alternative to oxine which has been associated with solubility and toxicity issues [42-45] as the ionophore for  $^{111}\text{In}^{3+}$  shuttling into the exosomal lumen. The second method involved covalently attaching DTPA-anhydride, a bifunctional chelator on the exosome surface that confers them the ability to bind  $^{111}\text{In}^{3+}$  stably. Although both of these approaches have been used to radiolabel cells, the properties of exosomes labelled by these means have not previously been evaluated. Therefore, the radiolabelling efficiency and stability of both approaches were assessed, and the approach with the most favourable outcome was used to study the biodistribution of melanoma-derived exosomes in both immunocompetent and immunodeficient melanoma bearing mice, to investigate the effect of the mouse immune system on exosome biodistribution.

## Materials

Sterile Newborn Calf Serum Heat Inactivated was purchased from First Link (UK). Millex-GP Syringe Filter Units 0.22  $\mu\text{m}$  were purchased from Merck Millipore (UK). Copper 300-mesh grid was purchased from Elektron Technologies (UK). Sodium chloride and glycine were purchased from VWR Chemicals (UK). CELLine AD1000 bioreactor flasks was purchased from Wheaton (UK). Indium-111 chloride was purchased from Mallinckrodt (NL). Sepharose® CL-2B was purchased from GE Healthcare Life Sciences (UK). Sucrose, chloroform, magnesium sulphate and acetic acid were purchased from Fisher Scientific (UK). Ammonium acetate was purchased from Santa Cruz Biotechnology (UK). Thin layer chromatography (TLC) papers were purchased from Agilent Technologies UK Ltd (UK). Isoflurane (IsoFlo®) for anaesthesia was purchased from Abbott Laboratories (UK). PBS pH 7.4 10X, Advanced RPMI, penicillin/Streptomycin, GlutaMax™ 100X, Trypsin-EDTA 0.05%, aldehyde/sulfate latex beads 4% w/v 4  $\mu\text{m}$  and Micro BCA™ kit were purchased from Thermo Fisher Scientific (UK). Deuterium oxide, tropolone, diethylenetriaminepentaacetic dianhydride (DTPA-anhydride), Trypan blue 0.4%, D-(+)-Glucose 10%, Laminin, DMEM Nutrient Mixture F-12 Ham, BSA and HEPES buffer were purchased from Sigma-Aldrich (UK). Anti-CD81 and anti-CD9 polyclonal primary antibodies were purchased from Bioss antibodies (USA). Goat anti-rabbit secondary antibody Cy5-conjugated was purchased from Abcam (UK).

## **Methods**

### **Cell culture conditions**

The murine melanoma B16F10 cells were cultured in Advanced RPMI 1640 medium supplemented with either 10% normal or exosome-depleted FBS, 1% penicillin/streptomycin and 1% GlutaMax™ in CELLline AD1000 bioreactor flasks. Exosome-depleted FBS was prepared by subjecting FBS to ultracentrifugation at 100,000 g for 18 h at 4°C. The FBS supernatant post-centrifugation was collected and sterile-filtered using 0.22 µm filters for use in cell culture. Cells from 4 x T75 flasks (80% confluent) in 15 ml medium supplemented with 10% exosome-depleted FBS were seeded into the cell compartment of 1 bioreactor flask. The medium reservoir compartment of the flask was filled with 500 ml of the medium supplemented with 10% normal FBS. Culture supernatant or conditioned medium (CM) was harvested from the cell compartment of the flask on a weekly basis and replaced with 15 ml of fresh medium supplemented with 10% exosome-depleted FBS. Collected CM was stored at 4°C until used for exosome isolation.

### **Exosome isolation**

B16F10 CM was pre-cleared of dead cells and cellular debris by several rounds of differential centrifugation: 500 g for 5 minutes at 4°C (twice), then at 2000 g for 15 minutes; followed by filtration through 0.22 µm filter. Pre-cleared CM (22.5 ml) was added to polycarbonate ultracentrifuge tubes (355631, Beckman Coulter). Sucrose solution (25% w/w in D<sub>2</sub>O, 3 ml) was then carefully added to the bottom of the CM using glass pipettes. The ultracentrifuge tubes were placed in a swing-out rotor (SW45 Ti, Beckman Coulter) and subjected to ultracentrifugation at 100,000 g for 90 min at 4°C (Optima™ XPN-80, Beckman Coulter). Post-centrifugation, the sucrose solution (2 ml) was withdrawn and added to 20 ml filtered PBS in polycarbonate ultracentrifuge bottles (355618), Beckman Coulter), and subjected to another round of ultracentrifugation in a fixed-angle rotor (Type 70 Ti, Beckman Coulter) at 100,000 g for 90 min at 4°C. The pellet obtained was resuspended in 400 µl filtered PBS.

## **Nanoparticle Tracking Analysis (NTA) and protein measurements**

Exosome hydrodynamic size and number were measured by Nanoparticle Tracking Analysis (NTA) using NanoSight LM10 (Malvern Instruments, UK). The exosome sample was first diluted in filtered PBS to obtain 20-80 particles in the viewing frame. The modal size and particle count were measured in triplicates, with 30 s as the duration for each recording, and analysed using the NanoSight NTA 3.2 software (Malvern Instruments, UK). The results were expressed as mean  $\pm$  standard deviation (SD). Protein measurements were measured using Micro BCA™ kit.

## **Flow cytometry**

Exosomes were coupled to latex microbeads using a protocol adapted from Théry et al. [46] prior to the detection of exosomal surface markers with flow cytometry. Briefly, 40  $\mu$ l of exosomes were incubated with 10  $\mu$ l aldehyde/sulphate latex beads for 15 min at room temperature (RT) before 5  $\mu$ l of 100  $\mu$ M BSA solution was added to the exosome-bead mixture (10  $\mu$ M final concentration). This was followed by incubation in 1 ml glycine (100 mM in PBS) for 30 min at RT, after which it was centrifuged for 5 min at 580 g and washed twice with 1 ml of 3% exosome-depleted FBS (made in PBS, henceforth referred to as 3% FBS/PBS). After the second wash, the pellet was resuspended in 3% FBS/PBS and stained with CD81 and CD9 antibodies respectively (rabbit anti-mouse) followed by the Cy5-conjugated secondary antibody (45 min each at 4°C). The bead/exosome complexes were washed once with 1 ml 3% FBS/PBS after incubation with each antibody, and the pellet resuspended in an appropriate volume of 3% FBS/PBS. The exosome-bead complex was run on FACSCalibur using FL4 channel for detection of Cy5 signals, and the results were analysed using CellQuest Pro software (BD Biosciences, US). A control sample consisting of beads only was prepared and subjected to the same treatment as the above but without staining.

## **Transmission and scanning electron microscopy**

For transmission electron microscopy (TEM), a sample of exosomes was fixed in formaldehyde/glutaraldehyde (2.5% each in 0.1 M sodium cacodylate buffer, pH 7.4) for 15 min. The sample was then placed on 300-mesh carbon-coated copper grids and left

to air-dry. Negative staining was achieved using filtered aqueous uranyl acetate (25% in methanol) for 4 min followed by two 50% methanol/H<sub>2</sub>O washes and left to air-dry. The grids were imaged using Philips CM 12 (FEI Electron Optics, NL) equipped with Tungsten filament and a Veleta – 2k x 2k side-mounted TEM CCD camera (Olympus, Japan) with the following settings: accelerating voltage – 80 kV; spot size – 2; objective aperture – 150 μm.

For scanning electron microscopy (SEM), a sample of exosomes was fixed in 5% glutaraldehyde for 2 h, which was then added on the surface of APTES pre-treated silicon wafer and left for 1 h. This was followed by washing with PBS three times and dehydrated in a series of increasing ethanol concentrations (20, 50, 70, 90, 95, 100%). The samples were transferred for critical drying (Samdri, Tousimis), and sputter coated with gold before scanning. SEM was performed on FEI Inspect-F (Philips, Eindhoven, NL) operated at 20 kV.

### **Intraluminal radiolabelling of exosomes ([<sup>111</sup>In]-Exo<sub>B16</sub>)**

Tropolone was dissolved in 200 mM HEPES buffered saline (HBS) pH 7-7.5 to make 1 mg/ml stock solution. 70-100 MBq <sup>111</sup>InCl<sub>3</sub> was added to 2 μg (2 μl) tropolone from the stock solution allowing for the [<sup>111</sup>In]Tropolone complex to form. The [<sup>111</sup>In]Trop mixture was added to exosomes (1 x 10<sup>11</sup> particles/mouse) diluted with PBS to achieve a final tropolone concentration of 5 μg/ml and incubated for 20 min at 37°C. Radiolabelled exosomes ([<sup>111</sup>In]-Exo<sub>B16</sub>) were purified from free [<sup>111</sup>In]Trop complex by gel filtration using Sepharose® CL-2B as the resolving matrix, self-packed according to the dimensions of the commercially available NAP-5™ columns, and optimised such that exosomes will elute in the first 2 x 500 μl fractions (F1 and F2). Radiolabelling efficiency was calculated as follows:

$$\text{Radiolabelling efficiency (\%)} = \frac{\text{Activity recovered in F1 + F2}}{\text{Initial activity used}} \times 100$$

## Membrane radiolabelling of exosomes ( $[^{111}\text{In}]\text{DTPA-Exo}_{\text{B16}}$ )

DTPA-anhydride was added to dry chloroform (prepared by adding magnesium sulphate powder to chloroform and stirring the mixture vigorously for 2 min, and then filtered to remove the powder) to form a suspension at a concentration of 1  $\mu\text{g}/\mu\text{l}$ , with brief sonication to break visible clumps. The amount required for the reaction with exosomes was added into a microtube and passed under a nitrogen stream to evaporate the chloroform thus forming a thin film of DTPA-anhydride on the lining of the microtube. Exosomes ( $1 \times 10^{11}$  particles/mouse in 100  $\mu\text{l}$ ) were added to the DTPA-anhydride film at a molar ratio of 1:400 (lysine on exosome:anhydride – it was assumed that 1 exosome is equivalent to 1 BSA molecule i.e. containing 59 lysine residues) and incubated at 37°C for 30 min. Excess unreacted DTPA-anhydride was purified using Sepharose® CL-2B columns as described above. 15-50 MBq of  $^{111}\text{InCl}_3$  was added to 0.2 M ammonium acetate buffer (pH 5.5) to achieve a final volume of 500  $\mu\text{l}$ . This was then added to an equal volume of DTPA-Exo<sub>B16</sub> to achieve a final concentration of 0.1 M ammonium acetate buffer (pH 5.5). The mixture was incubated for 5 min at RT. Radiolabelled exosomes ( $[^{111}\text{In}]\text{DTPA-Exo}_{\text{B16}}$ ) were purified from excess  $^{111}\text{InCl}_3$  using Sepharose® CL-2B columns, and the radiolabelling efficiency then determined as described above.

## Radiochemical stability assessment

### *Intraluminal-labelled exosomes*

$[^{111}\text{In}]\text{-Exo}_{\text{B16}}$  was incubated in 50% FBS or PBS (1:1, v/v) for 24 h at 37°C. Samples post-incubation were passed through Sepharose® CL-2B columns and the first 2 x 500  $\mu\text{l}$  fractions (F1 and F2) were collected as described earlier. Radiochemical stability of  $[^{111}\text{In}]\text{-Exo}_{\text{B16}}$  was calculated as follows:

$$\text{Radiochemical stability (\%)} = \frac{\text{Activity recovered in F1 + F2}}{\text{Sample activity post-incubation}} \times 100$$

### *Membrane-labelled exosomes*

[<sup>111</sup>In]DTPA-Exo<sub>B16</sub> was incubated in 50% FBS or PBS as described above, and samples post-incubation were then spotted on thin layer chromatography (TLC) paper strips impregnated with silica gel. The strips were eluted with 0.1 M ammonium acetate containing 0.25 mM EDTA (pH 5.5) and analysed on a phosphor imager (Cyclone® Packard, Australia). The percentage of <sup>111</sup>In still attached to exosomes (immobile spot at the application point) was considered as the radiochemically stable [<sup>111</sup>In]DTPA-Exo<sub>B16</sub>.

### **Animal models**

All animal experiments were performed in compliance with the UK Home Office Animals (Scientific Procedures) Act 1986. Female C57Bl/6 mice and male NOD SCID gamma (NSG) mice (~20 g, 6-8 weeks old) were obtained from Charles River (UK). Subcutaneous (SC) tumours were established by inoculating B16F10 cells (1 × 10<sup>6</sup> cells in 100 µl PBS) subcutaneously into the left and right rear flanks of the mice. The mice were monitored closely post-inoculation and were used for studies when the tumours reached ~200-300 mm<sup>3</sup>.

### **Whole body SPECT/CT imaging of radiolabelled exosomes**

For intraluminal-labelled exosomes, C57Bl/6 mice (n=1 per treatment) was injected intravenously *via* the tail vein with 1 × 10<sup>11</sup> [<sup>111</sup>In]-Exo<sub>B16</sub> (5-10 MBq) or the equivalent amount of radioactivity of free [<sup>111</sup>In]Trop. For membrane-labelled exosomes, C57Bl/6 mice (n=1 per treatment) was injected with 1 × 10<sup>11</sup> [<sup>111</sup>In]DTPA-Exo<sub>B16</sub> (5 – 10 MBq) or the equivalent amount of radioactivity of free [<sup>111</sup>In]DTPA. Mice were imaged under anaesthesia (2% isoflurane in air) in prone position on a heating pad at 37°C using a nanoSPECT/CT four-head scanner (Bioscan, USA). SPECT images were obtained at 0-30 min, 4 h and 24 h post-injection using 1.4 mm pinhole collimators (24 projections, 60 s per projection; 30 min scan) and CT images were obtained at the end of each SPECT acquisition using an X-ray source setting of 45 kVp. All data were reconstructed with proprietary Bioscan software and SPECT and CT acquisitions were fused using PMOD® software (Mediso). Mice were culled and disposed of after the 24 h imaging.

### **Ex vivo gamma counting of excised organs/tissue**

Similar to SPECT/CT imaging, mice were injected intravenously with  $1 \times 10^{11}$  [ $^{111}\text{In}$ ]-EXO<sub>B16</sub> (0.5 – 1 MBq) or free [ $^{111}\text{In}$ ]Trop of equivalent radioactivity; and  $1 \times 10^{11}$  [ $^{111}\text{In}$ ]DTPA-EXO<sub>B16</sub> (0.5 – 1 MBq) or free [ $^{111}\text{In}$ ]DTPA of equivalent radioactivity. Blood samples (5  $\mu\text{l}$  from the tail vein) were taken at various time points (2, 5, 10, 30, 60, 240 and 1440 min) to analyse the exosome circulation profile. Urine and faeces were collected by housing the mice in metabolic cages for 24 h to analyse the excretion profile. After 1, 4 and 24 h, mice were sacrificed (n=3 per time point) and perfused with heparinised saline (1000U/l, 25 ml per animal). Major organs (brain, lungs, liver, spleen, kidneys, heart, and stomach), muscle, skin, bone (femur), carcass and tumours were collected, weighed and placed in scintillation vials. Samples were counted in a gamma counter (LKB Wallac 1282 Compugamma, PerkinElmer, UK) together with radioactive dose standards. Radioactivity readings (counts per minute – CPM) were expressed as percentage of injected dose per organ (%ID/organ) or percentage of injected dose per gram of tissue (%ID/gT). Data were expressed as the mean  $\pm$  SD of sample triplicates.

### **Statistical analyses**

For all experiments, data were presented as mean  $\pm$  SD, where n denotes the number of repeats. Statistical significance of the data was assessed using Student's t-test and is designated with asterisk(s) ( $p^* < 0.05$ ,  $p^{**} < 0.01$ , and  $p^{***} < 0.001$ ).

# Results

## Exosome isolation and physicochemical characterisation

Cancer cell lines are known to be good exosome producers [3-6] and hence they were selected as exosome sources in this study. Exosomes were isolated from B16F10 cells (murine melanoma) cultured in a bioreactor flask (CELLine AD1000) which can help increase the yield of exosomes [47]. The culture supernatant, hereby referred to as conditioned medium (CM) was harvested on a weekly basis. CM initially underwent pre-clearing to remove dead cells and cellular debris by a series of differential centrifugation and ultrafiltration. Pre-cleared CM was then subjected to ultracentrifugation onto a sucrose cushion to separate exosome from proteins by density in the CM, followed by a washing step to remove the sucrose and residual contaminating proteins. The resulting exosome pellet was resuspended in a small volume of PBS (400  $\mu$ l) to make a concentrated exosome stock.

The physicochemical characterisation of exosomes isolated from B16F10 (Exo<sub>B16</sub>) cells are summarised in **Table 1**. The size measured using NanoSight was  $132.3 \pm 5.6$  nm, which compares to other exosome studies. Particle concentration quantification (also using NanoSight) showed that B16F10 cells are a prolific exosome producer, yielding  $1.02 \times 10^{13} \pm 3.9 \times 10^{12}$  p/ml from 72 ml of CM (obtained from 6 rounds of CM collection from a single bioreactor flask). A measure of purity of the Exo<sub>B16</sub> from contaminating proteins was also carried out by means of calculating the particle to protein (P:P) ratio of the isolated exosome stock. The P:P ratio was found to be  $4.52 \times 10^{10} \pm 1.26 \times 10^{10}$  p/ $\mu$ g protein, which falls in the proposed range of high purity level [47].

## Biochemical and morphological analysis of Exo<sub>B16</sub>

Detection of exosomal markers was achieved using flow cytometry as previously described [48]. The isolated Exo<sub>B16</sub> expressed CD81 and CD9, which is a common property of exosomal vesicles (**Fig. 1A** and **Fig. S1**). Morphological analysis of Exo<sub>B16</sub> was also undertaken using both transmission electron microscopy (TEM) and scanning electron microscopy (SEM), which can also validate the size measurement obtained from

NanoSight. Both TEM and SEM images of Exo<sub>B16</sub> demonstrated that the exosomes were spherical structures slightly above 100 nm in size (**Fig. 1B**).

**Table 1 Physicochemical characterisation of exosomes**

Exosome	Size <sup>1,2</sup> (nm)	Yield <sup>1,2,3</sup> (p/ml)	[Protein] <sup>2,4</sup> (ug/mL)	Particle to protein (P:P) ratio <sup>2,5</sup> (p/ug)
B16F10	132.3 ± 5.6	2.04x10 <sup>13</sup> ± 3.9x10 <sup>12</sup>	451.15 ± 71.5	4.52x10 <sup>10</sup> ± 1.26 x10 <sup>10</sup>

1 Measured using NanoSight LM10

2 Values are expressed as mean ± SD, where n=3

3 Yield was obtained by cell-conditioned medium pooled from 6 rounds of harvesting from CELLLine AD1000 flasks (72 ml)

4 Measured using BCA assay

5 Value obtained by using formula: P:P ratio = Yield / [Protein]

## Intraluminal radiolabelling of Exo<sub>B16</sub>

### *Radiolabelling efficiency and stability*

The intraluminal radiolabelling approach is achieved *via* the ability of the small hydrophobic molecule called tropolone to chelate radionuclides and form a complex that allows the radionuclide to diffuse across the exosomal membrane and into the exosomal lumen, similar to its predecessor oxine [49]. This method, particularly utilising the <sup>111</sup>Indium-tropolone complex ([<sup>111</sup>In]Trop) has been widely used to radiolabel cellular components of blood such as platelets [42, 43], lymphocytes [44, 50] and granulocytes [51] for *in vivo* imaging. Other cell types such as mesenchymal stem cells [52, 53] and endometrial cells [54] have also been successfully radiolabelled using [<sup>111</sup>In]Trop. More recently, [<sup>111</sup>In]Trop was used to label polymeric micelles [55]. The orientation of exosomal transmembrane proteins is the same as their parent cells [14] and therefore provides the opportunity for them to be radiolabelled using the same principle. The mechanism by which this intraluminal radiolabelling is achieved is summarised in **Scheme 1A**. Tropolone is firstly mixed with <sup>111</sup>Indium (as <sup>111</sup>InCl<sub>3</sub>) to allow for the formation of the [<sup>111</sup>In]tropolone complex. The chemical structure of tropolone and [<sup>111</sup>In]Trop complex is illustrated in **Scheme S1A** and **S1B** (supplementary information).

Upon incubation with exosomes, [ $^{111}\text{In}$ ]Trop gets translocated into the exosomal lumen, forming the intermediate [ $^{111}\text{In}$ ]Trop-Exo<sub>B16</sub>. Upon entry,  $^{111}\text{In}^{3+}$  exchanges to bind with cytoplasmic biomolecules of at least 3.6 kDa [49]. As the interaction between  $^{111}\text{In}^{3+}$  and tropolone is not particularly strong,  $^{111}\text{In}^{3+}$  from the [ $^{111}\text{In}$ ]Trop will then exchange with proteins and nucleic acids within the exosomal lumen [49]. Free tropolone molecules leave the exosomal lumen and the  $^{111}\text{In}^{3+}$  is now entrapped within the lumen, thereby resulting in radiolabelled exosomes ([ $^{111}\text{In}$ ]-Exo<sub>B16</sub>).

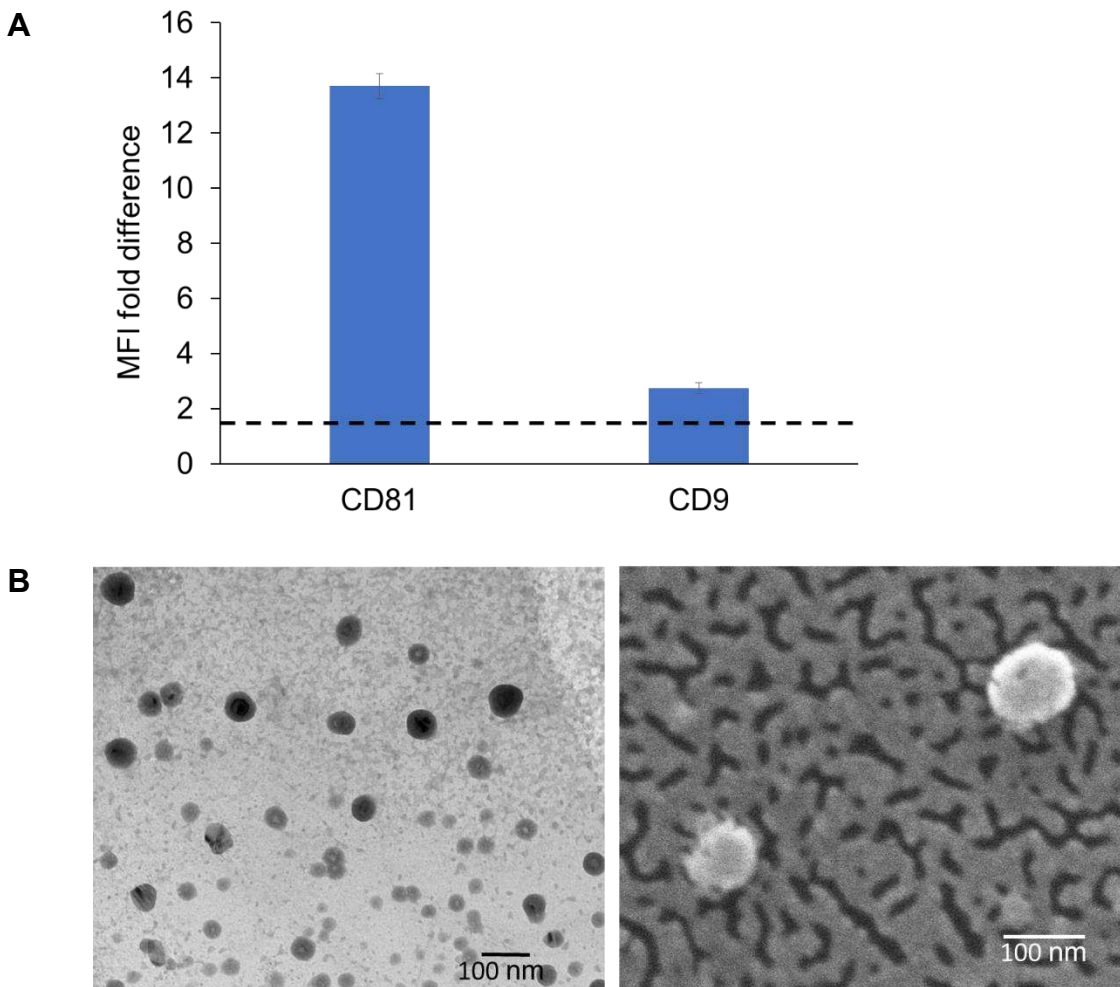
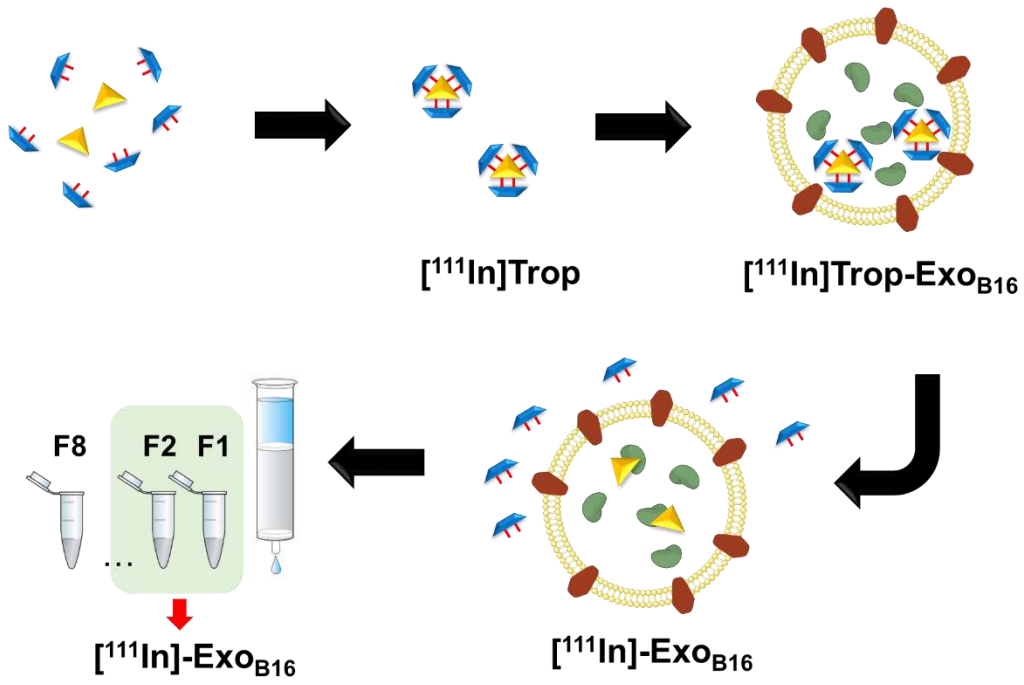
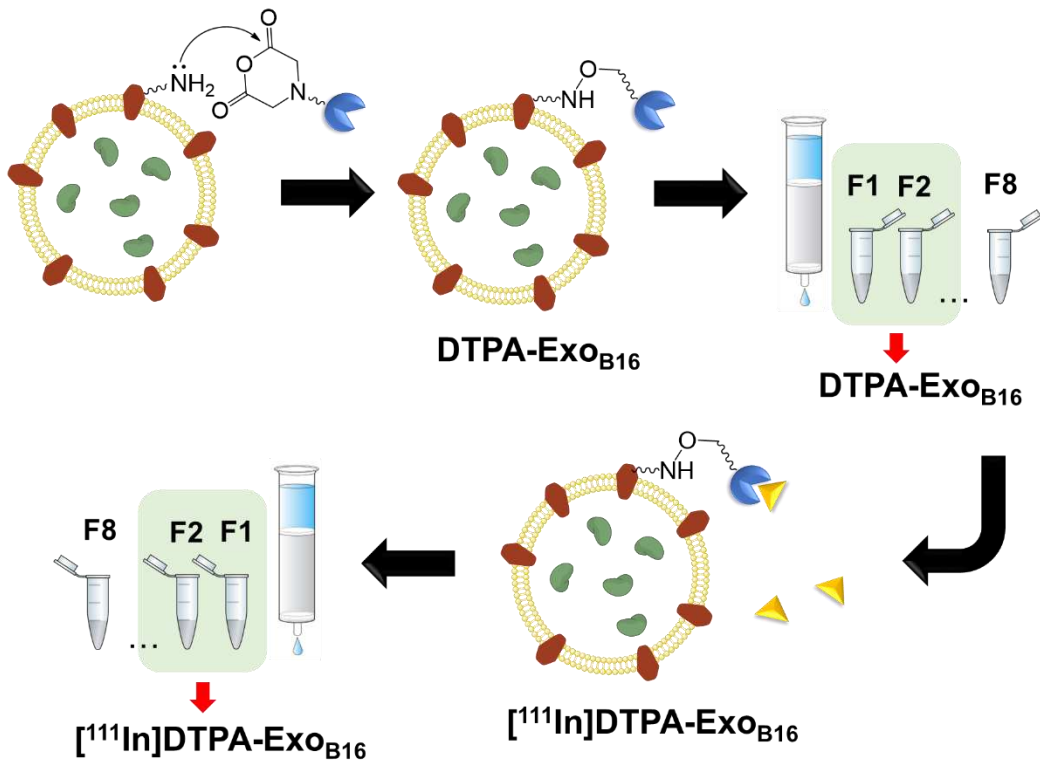


**Fig. 1 Biochemical and morphology analysis of B16F10 exosomes. (A)** Detection of exosomal markers CD81 and CD9 using flow cytometry on exosomes isolated from B16F10 cells. Exosomes were coupled to aldehyde/sulphate latex beads prior to detection. Exo-beads complex were subsequently stained using a 2-step labelling (anti-CD81 or anti-CD9 1° ab/Cy5-conjugated 2° ab). Degree of expression of the markers are expressed as the fold difference in median fluorescence intensity (MFI) values from that of the control (exo-beads complex stained with Cy5-conjugated 2° ab). Values are expressed as mean  $\pm$  SD, where n=3. **(B)** Transmission electron microscopy (TEM) and scanning electron microscopy (SEM) images of exosomes isolated from B16F10 cells.

A



B



<b>Key:</b>	$^{111}\text{In}^{3+}$	Tropolone	$[^{111}\text{In}]\text{Trop}$	DTPA-anhydride	Exosome
-------------	------------------------	-----------	--------------------------------	----------------	---------

Scheme 1 (A) Intraluminal and (B) membrane radiolabelling protocols of B16F10 exosomes

Purification of excess [ $^{111}\text{In}$ ]Trop from [ $^{111}\text{In}$ ]-Exo $_{\text{B16}}$  was carried out *via* gel filtration using Sepharose® CL-2B as the resin. Free [ $^{111}\text{In}$ ]Trop was used as a control and the elution profiles of both [ $^{111}\text{In}$ ]-Exo $_{\text{B16}}$  and [ $^{111}\text{In}$ ]Trop were analysed. Exosomes were found to elute in F1 and F2 (**Fig. S2A and S2B**) while [ $^{111}\text{In}$ ]Trop mainly eluted in F4 and F5 (**Fig. 2A**). The percentage (%) radiolabelling for [ $^{111}\text{In}$ ]-Exo $_{\text{B16}}$  was  $4.73 \pm 0.39\%$  compared to only  $0.20 \pm 0.04\%$  ( $p < 0.05$ ) for [ $^{111}\text{In}$ ]Trop collected in F1+F2 (**Fig. 2A**).

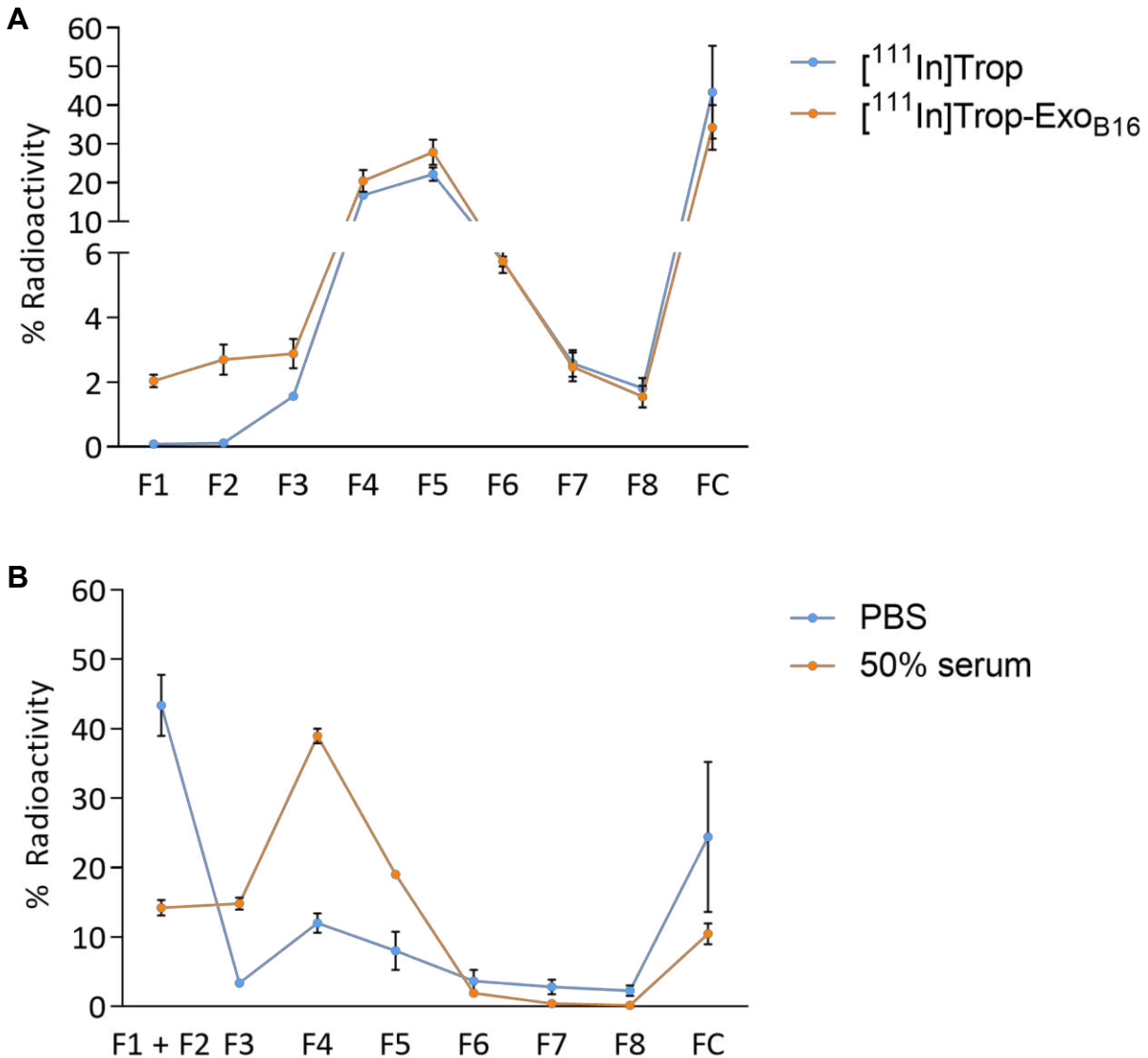


**Fig. 2 Radiolabelling efficiency and radiochemical stability of intraluminal-labelled B16F10 exosomes.** (A) Radiolabelled exosomes ([ $^{111}\text{In}$ ]-Exo $_{\text{B16}}$ ) were purified from excess [ $^{111}\text{In}$ ]Trop complex by gel filtration (Sepharose® CL-2B). Eight 500  $\mu\text{l}$  fractions were collected and the radioactivity for each fraction and the column itself post-purification was measured by gamma counting, and are expressed as the percentage of activity relative to the initial activity

added to the column. Radiolabelling efficiency was calculated as the sum of % radioactivity recovered from F1 and F2. **(B)** Radiolabelled exosomes were incubated in either PBS or 50% serum for 24 h at 37°C, and then passed through the same column as **(A)**. Eight 500 µl fractions were collected and the radioactivity for each fraction and the column itself (FC) post-purification was measured using gamma counter, and are expressed as the percentage of activity relative to the activity of the sample added to the column. Radiochemical stability was calculated as the sum of % radioactivity recovered from F1 and F2. Values are expressed as mean ± SD, where n=3. Statistical analysis was done on F1 and F2 ( $p^* < 0.05$ ,  $p^{***} < 0.001$ ).

[<sup>111</sup>In]-Exo<sub>B16</sub> were incubated in either PBS or 50% serum at 37°C for 24 h to assess the radiochemical stability of the labelling. The typical method of assessing the labelling stability is using thin layer chromatography (TLC), by measuring the % activity that did not migrate with the mobile phase and remains at the application point after 24 h incubation, corresponding to radiolabelled macromolecules [56-58]. It was not possible to apply this method to assess the intraluminal labelling stability of exosomes as [<sup>111</sup>In]Trop will not migrate using 0.1 M ammonium acetate with 0.25 mM EDTA, pH 5.5 mobile phase, rendering it impossible discern whether the % activity remaining at the application point is originating from that of radiolabelled exosomes or free [<sup>111</sup>In]Trop. An alternative approach was used by passing sample post-incubation through Sepharose® CL-2B column used previously to determine radiolabelling efficiency. The stability of intraluminal-labelled [<sup>111</sup>In]-Exo<sub>B16</sub> was found to be 43.35 ± 10.12% and 14.21 ± 2.76% in PBS and 50% serum, respectively, at 24 h post incubation (**Fig. 2B**).

Biodistribution of intraluminal-labelled [<sup>111</sup>In]-Exo<sub>B16</sub> was assessed qualitatively and quantitatively using whole body SPECT/CT imaging and *ex vivo* gamma counting, respectively. Significant difference was observed in the organ accumulation profile of [<sup>111</sup>In]-Exo<sub>B16</sub> as compared to that of free [<sup>111</sup>In]Trop, which further supports the successful radiolabelling of the exosomes (**Fig. S3, S4 and S5**). However, due to the low stability of the intraluminal-labelled [<sup>111</sup>In]-Exo<sub>B16</sub>, the reliability and accuracy of the organ accumulation values, especially that of the tumours were deemed improbable.

## Membrane radiolabelling of Exo<sub>B16</sub>

### *Radiolabelling efficiency and stability*

Membrane radiolabelling was achieved by covalently attaching the bifunctional chelator DTPA-anhydride to the exosome surface in an amine-dependent reaction. Exosome membranes contain various transmembrane proteins which are likely to have free amines (from lysine residues) on the extraluminal domain. The schematics of the reaction are summarised in **Scheme 1B**. The free amines act as nucleophiles that attack anhydrides on the DTPA, resulting in exosomes with covalently attached DTPA on their surface *via* amide bonds (DTPA-Exo<sub>B16</sub>). Incubating DTPA-Exo<sub>B16</sub> with <sup>111</sup>Indium (as <sup>111</sup>InCl<sub>3</sub>) will then allow <sup>111</sup>In<sup>3+</sup> to be chelated by DTPA on the exosomes, thereby radiolabelling the exosomes ([<sup>111</sup>In]DTPA-Exo<sub>B16</sub>). The chemical structure of DTPA-anhydride and its reaction with exosomal amine is illustrated in **Scheme S1C** and **S1D** respectively (supplementary information).

Radiolabelling efficiency of membrane-labelled exosomes was assessed in a similar manner to that of intraluminal labelling, where [<sup>111</sup>In]DTPA and [<sup>111</sup>In]DTPA-Exo<sub>B16</sub> were eluted through Sepharose® CL-2B columns and their respective elution profiles analysed. Radiolabelling efficiency was determined as the % radioactivity recovered in F1+F2. [<sup>111</sup>In]DTPA and [<sup>111</sup>In]DTPA-Exo<sub>B16</sub> showed similar elution profile, but unlike that observed with intraluminal labelling, % activity eluted in F4 and F5 were less than that of F1 and F2, with higher % activity being retained in the column post-elution (**Fig. 3A**). Percentage (%) activity recovered in F1+F2 for [<sup>111</sup>In]DTPA-Exo<sub>B16</sub> was significantly higher than that of [<sup>111</sup>In]DTPA (19.2 ± 4.53% and 0.02 ± 0.001% respectively), thereby confirming that the activity recovered in F1+F2 were from [<sup>111</sup>In]DTPA-Exo<sub>B16</sub>. The radiolabelling efficiency of [<sup>111</sup>In]DTPA-Exo<sub>B16</sub> considered to be 19.2 ± 4.53 % was significantly higher than that obtained by intraluminal-labelling method (**Fig. 2A**).

Radiochemical stability of [<sup>111</sup>In]DTPA-Exo<sub>B16</sub> in PBS and 50% serum after 24 h at 37°C was assessed using TLC as explained above, by measuring the % activity that did not migrate with the mobile phase (0.1 M ammonium acetate with 0.25 mM EDTA, pH 5.5) and remained at the application point, corresponding to radiolabelled exosomes. Free In<sup>3+</sup> was also run on the TLC paper as a control, where they all migrate to the solvent

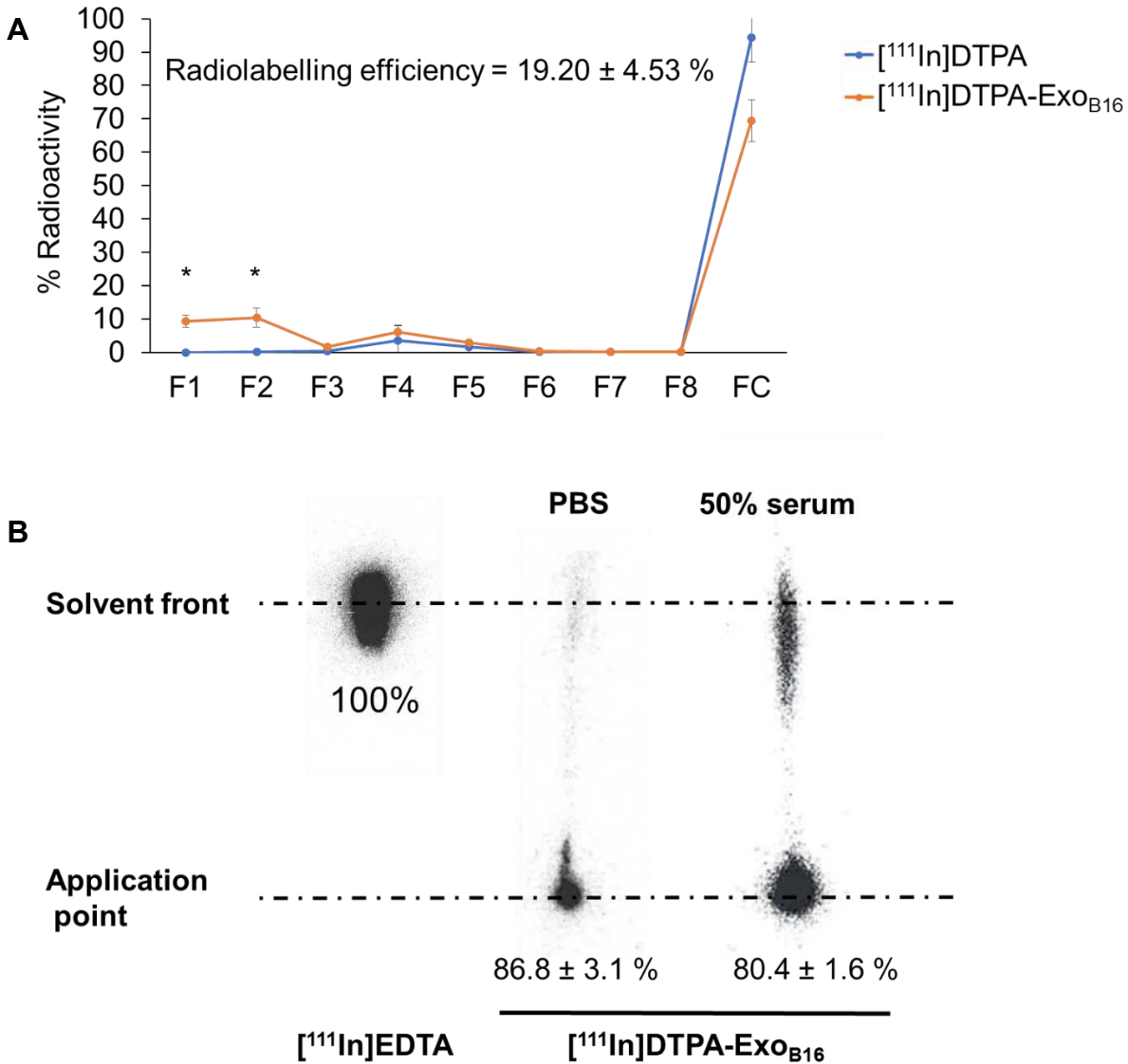


**Fig. 3 Radiolabelling efficiency and radiochemical stability of membrane-labelled B16F10 exosomes.** (A) B16F10 exosomes with covalently attached DTPA (DTPA-Exo<sub>B16</sub>) were purified from excess <sup>111</sup>InCl<sub>3</sub> by gel filtration (Sepharose® CL-2B). Eight 500 µl fractions were collected and the radioactivity for each fraction and the column itself post-purification was measured by gamma counting, and are expressed as the percentage of activity relative to the initial activity added to the column. Radiolabelling efficiency was calculated as the sum of % radioactivity recovered from F1 and F2. Values are expressed as mean ± SD, where n=3. Statistical analysis was done on F1 and F2 ( $p^{**} < 0.01$ ,  $p^{***} < 0.001$ ). (B) Radiolabelled exosomes ([<sup>111</sup>In]DTPA-Exo<sub>B16</sub>) were incubated in either PBS or 50% serum for 24 h at 37°C, and then spotted on a TLC paper. The paper was then run on 0.1 M ammonium acetate with 0.25mM EDTA (pH 5.5) as the mobile phase and imaged using a phosphorimager. Radiochemical stability was calculated as % radioactivity remaining at the application point. Values are expressed as mean ± SD, where n=3.

front as they were chelated by EDTA present in the mobile phase (**Fig. 3B**). The stability of [ $^{111}\text{In}$ ]DTPA-Exo<sub>B16</sub> in PBS and 50% serum was ~87 % and ~80% respectively, both higher than that of intraluminal-labelled exosomes (**Fig. 2B**).

#### *Whole body SPECT/CT live imaging*

[ $^{111}\text{In}$ ]DTPA and [ $^{111}\text{In}$ ]DTPA-Exo<sub>B16</sub> were injected intravenously into C57Bl/6 mice bearing subcutaneous B16F10 tumours ( $1 \times 10^{11}$  particles per animal for [ $^{111}\text{In}$ ]DTPA-Exo<sub>B16</sub>) for whole body SPECT/CT imaging, of which the former acts as a control to ensure the signals detected *in vivo* were coming from [ $^{111}\text{In}$ ]DTPA-Exo<sub>B16</sub> and not from free circulating [ $^{111}\text{In}$ ]DTPA that was cleaved from the exosome surface. Imaging was undertaken immediately, 4 h and 24 h post-injection. Imaging results showed a significant difference between the biodistribution profile of [ $^{111}\text{In}$ ]DTPA and [ $^{111}\text{In}$ ]DTPA-Exo<sub>B16</sub> (**Fig. 4**). At 0-30 min post-injection, high amounts of [ $^{111}\text{In}$ ]DTPA can be seen in kidneys and bladder indicating high urinary excretion, but at 4 h the signals can only be seen in the bladder, which then becomes too low to be detected at 24 h. In contrast, [ $^{111}\text{In}$ ]DTPA-Exo<sub>B16</sub> showed very high signals in the liver and spleen at 0-30 min post-injection, which remained up to 24 h. Some signals detected in the bladder at the earlier timepoints, and tumour accumulation was not observed. The clear distinction between the *in vivo* imaging results of [ $^{111}\text{In}$ ]DTPA and [ $^{111}\text{In}$ ]DTPA-Exo<sub>B16</sub> corroborated the finding that the % activity recovered in F1+F2 from **Fig. 3A** originated from labelled exosomes and confirms successful membrane radiolabelling of exosomes.

#### *Quantitative organ biodistribution by gamma counting*

Quantitative biodistribution analysis of both [ $^{111}\text{In}$ ]DTPA and [ $^{111}\text{In}$ ]DTPA-Exo<sub>B16</sub> at 1, 4 and 24 h was also carried out by gamma counting as per described above. Both [ $^{111}\text{In}$ ]DTPA and [ $^{111}\text{In}$ ]DTPA-Exo<sub>B16</sub> were found to be cleared rapidly from the circulation with only ~16.2% injected dose (ID) and ~10.5% ID respectively remaining after only 2 min post-injection and reaching a very low level of 1% or slightly less in just 1 h (**Fig. 5A**). Although both free [ $^{111}\text{In}$ ]DTPA and [ $^{111}\text{In}$ ]DTPA-Exo<sub>B16</sub> showed rapid clearance from the circulation, they showed significantly different kinetics especially in the earlier timepoints (<60 min). As expected, a significantly much higher amount of [ $^{111}\text{In}$ ]DTPA (~92.6% ID)

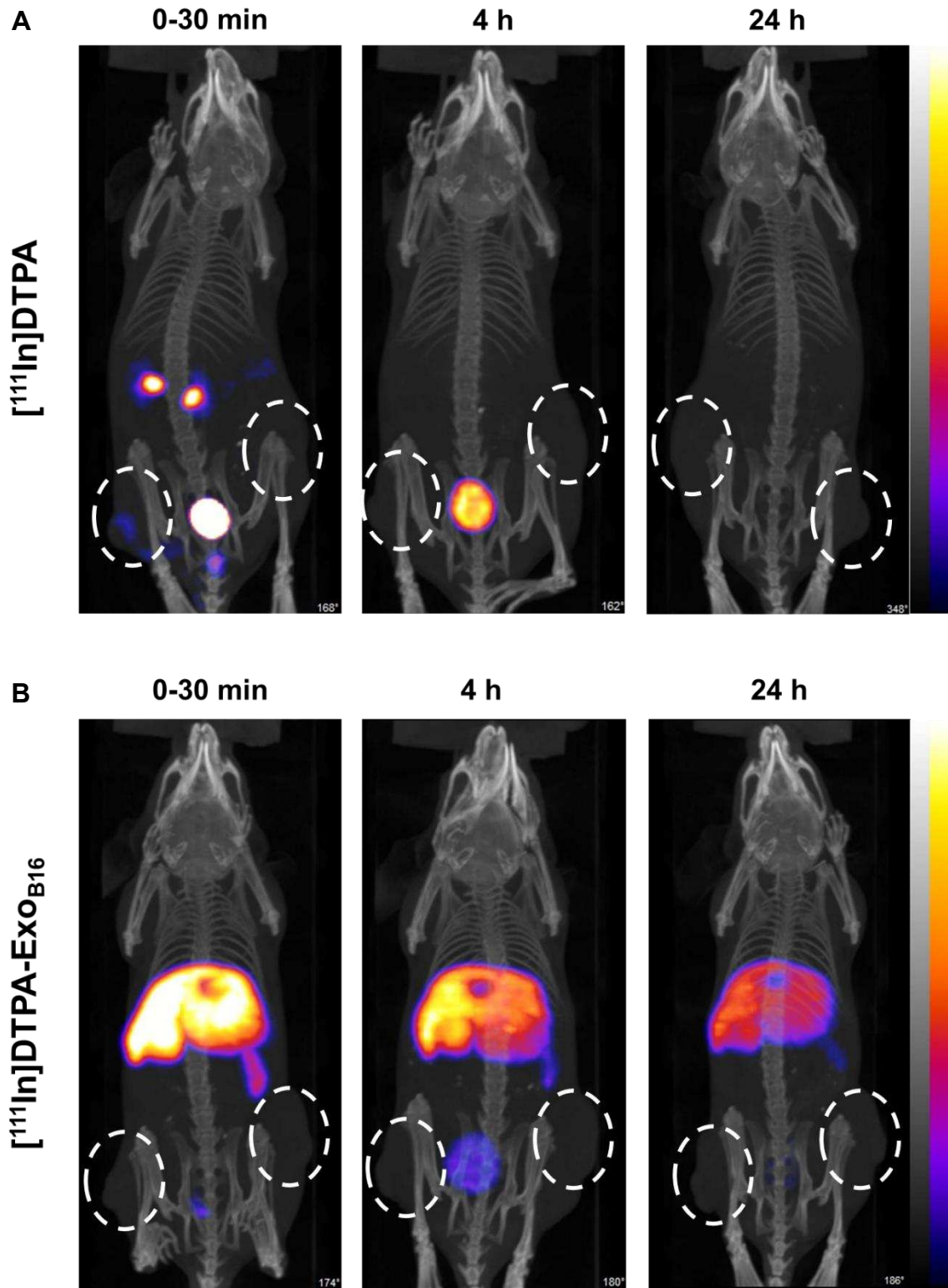


**Fig. 4** Whole body SPECT/CT imaging of membrane-labelled B16F10 exosomes in melanoma-bearing C57Bl/6 mice. (A) Animal was injected intravenously with free  $[^{111}\text{In}]\text{DTPA}$  complex as control. (B) Animal was injected with  $[^{111}\text{In}]\text{DTPA-Exo}_{\text{B16}}$ . Imaging was done immediately, 4, and 24 h post-injection. White circles indicate the position of tumours.

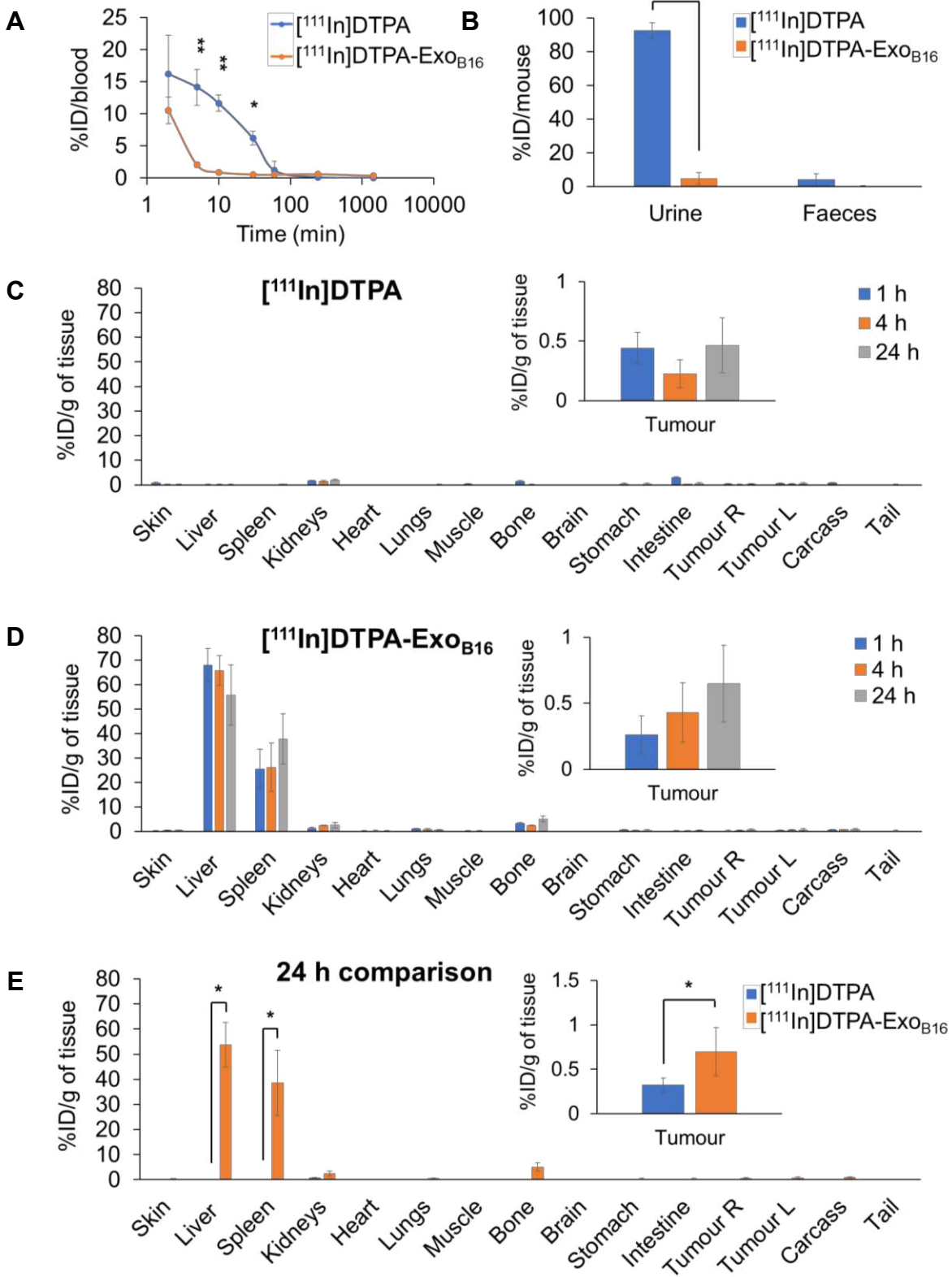


**Fig. 5** Blood circulation, excretion and organ biodistribution profiles of membrane-labelled B16F10 exosomes in melanoma-bearing C57Bl/6 mice. The  $[^{111}\text{In}]\text{DTPA}$  group was injected with 0.02M DTPA complexed with 0.5-1MBq of  $^{111}\text{InCl}_3$  while the  $[^{111}\text{In}]\text{DTPA-Exo}_{\text{B16}}$

Exo<sub>B16</sub> group was injected with  $1 \times 10^{11}$  [<sup>111</sup>In]DTPA-Exo<sub>B16</sub> (0.5-1MBq). **(A)** Blood circulation profile of [<sup>111</sup>In]DTPA and [<sup>111</sup>In]DTPA-Exo<sub>B16</sub>. 5 µl blood were taken *via* tail bleeding at 2 min, 5 min, 10 min, 30 min, 1 h, 4 h and 24 h following intravenous injection of each compound. **(B)** Excretion profile of [<sup>111</sup>In]DTPA and [<sup>111</sup>In]DTPA-Exo<sub>B16</sub> where urine and faeces were collected from the animals 24 h post-injection. **(C)** and **(D)** Organ biodistribution of [<sup>111</sup>In]DTPA and [<sup>111</sup>In]DTPA-Exo<sub>B16</sub> respectively. Animals were culled at 1 h, 4 h and 24 h post-injection, perfused with saline and their organs were excised for analysis by gamma counting. Inset shows the zoomed-in tumour accumulation values for each group. **(E)** Comparison of organ biodistribution of [<sup>111</sup>In]DTPA and [<sup>111</sup>In]DTPA-Exo<sub>B16</sub> 24 h post-injection, where inset shows zoomed-in tumour accumulation values for each group. Values are normalised to organ weight and expressed as mean  $\pm$  SD, where n=3 for each group. For **(C)**, **(D)** and **(E)**, statistical analyses were done on liver, spleen, kidneys and tumour ( $p^* < 0.05$ ,  $p^{**} < 0.01$ ,  $p^{***} < 0.001$ ).

was excreted in the urine as compared to that of [<sup>111</sup>In]DTPA-Exo<sub>B16</sub> (~4.93% ID), but the amount excreted in faeces was similarly low for both compounds with a value of ~1-4 % ID (**Fig. 5B**). Looking at organ biodistribution, there was minimal accumulation of [<sup>111</sup>In]DTPA with ~2.0 % ID per gram tissue (ID/gT) or lower across all organs including tumours, which recorded a value of about ~0.2 – 0.4 % ID/gT (**Fig. 5C**). In contrast, [<sup>111</sup>In]DTPA-Exo<sub>B16</sub> showed high accumulation in the liver with ~66.0% ID/gT at 1 and 4 h, which then decreased slightly to ~56.0 % ID/gT after 24 h, of which the difference is not significant (**Fig. 5D**). This was followed by spleen, which showed an accumulation of ~26.0% ID/gT at 1 and 4 h, which increased slightly but not significantly to ~37.7% ID/gT. Kidneys showed an accumulation of ~2.5 % ID/gT of [<sup>111</sup>In]DTPA-Exo<sub>B16</sub> after 24 h. Tumour accumulation of [<sup>111</sup>In]DTPA-Exo<sub>B16</sub> was initially very low but showed a steady increase, reaching a value of ~0.7 % ID/gT after 24 h. When comparing organ biodistribution values at 24 h, a significant difference can be observed between that of [<sup>111</sup>In]DTPA and [<sup>111</sup>In]DTPA-Exo<sub>B16</sub>, where the latter shows a significantly higher liver, spleen and tumour accumulation as compared to that of the former (**Fig. 5E**), which reflects successful and stable radiolabelling of Exo<sub>B16</sub>. The quantitative biodistribution results of both free [<sup>111</sup>In]DTPA and [<sup>111</sup>In]DTPA-Exo<sub>B16</sub> expressed as %ID/organ are summarised in **Fig. S6** (supplementary information). In summary, results from membrane-labelled exosomes, especially the quantitative organ accumulation values, were deemed as more reliable due to its superior radiochemical stability (thus higher signal-to-noise ratio) and is selected as the approach for the subsequent part of the study.

## Comparative biodistribution of Exo<sub>B16</sub> in immunocompetent and immunodeficient mice

Next, membrane-labelled exosomes were injected into NOD-*scid ILR2 $\gamma$ <sup>null</sup>* (NSG) mice to study the influence of the immune system on the *in vivo* biodistribution of exosomes. [<sup>111</sup>In]DTPA-Exo<sub>B16</sub> (1x10<sup>11</sup> particles per animal) were injected intravenously into NSG mice bearing subcutaneous B16F10 tumours and quantitative biodistribution analysis at 1, 4 and 24 h was carried out as the above *via* gamma counting. [<sup>111</sup>In]DTPA-Exo<sub>B16</sub> showed a similar blood circulation profile in NSG mice when compared to that in C57BL/6 mice, where [<sup>111</sup>In]DTPA-Exo<sub>B16</sub> was cleared rapidly from the circulation with only ~15.3% ID remaining at 2 min post-injection, which decreased to ~0.1% ID after 24 h (**Fig. 6A**). [<sup>111</sup>In]DTPA-Exo<sub>B16</sub> in NSG mice also showed similar amounts of excretion via the urine and faeces to that of C57BL/6 mice (**Fig. 6B**). [<sup>111</sup>In]DTPA-Exo<sub>B16</sub> in NSG mice also showed a similar pattern of organ accumulation to that in C57BL/6 mice across the time points, where the liver recorded the highest signals with ~48.3% ID/gT at 1 h, which then decreased slightly to ~40.0% ID/gT at 4 and 24 h (**Fig. 6C**). Spleen recorded the second highest accumulation of ~13.0 % ID/gT at 1 and 4 h, which then increased significantly to ~45.8 % after 24 h. [<sup>111</sup>In]DTPA-Exo<sub>B16</sub> accumulation in the kidneys showed a steady increase over the timepoints, reaching a value of ~6.8 % ID/gT after 24 h. The tumours showed an accumulation of around ~0.4 % ID/gT at 1 and 4 h, which then decreased slightly to ~0.3 % ID/gT after 24 h. Comparing biodistribution values at 24 h showed that [<sup>111</sup>In]DTPA-Exo<sub>B16</sub> accumulation in C57BL/6 and NSG mice recorded similar values across the different organs, especially in the liver, spleen and kidneys (**Fig. 6D**). [<sup>111</sup>In]DTPA-Exo<sub>B16</sub> in NSG mice however showed a significantly lower tumour accumulation as compared to that in C57BL/6 mice. In summary, exosomes show a similar pattern of organ accumulation in both immunocompetent and immunodeficient mouse models with the exception of tumour, in which the accumulation in the latter was lower.

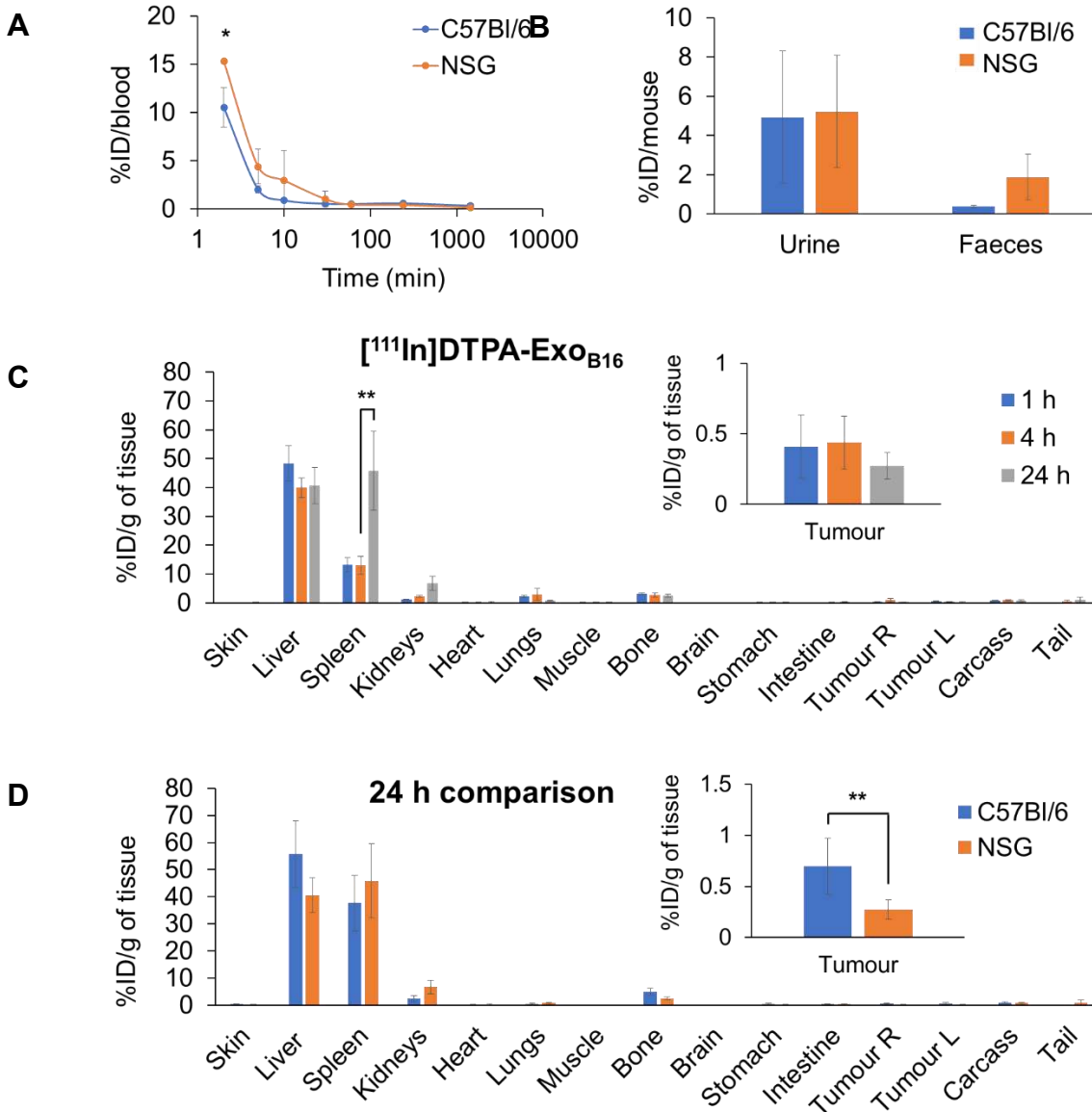


**Fig. 6 Blood circulation, excretion and organ biodistribution profile of membrane-labelled B16F10 exosomes in melanoma-bearing NSG mice.** Animals were injected with  $1 \times 10^{11}$   $[^{111}\text{In}]\text{DTPA-Exo}_{\text{B16}}$  (0.5-1MBq). **(A)** Blood circulation profile of  $[^{111}\text{In}]\text{DTPA-Exo}_{\text{B16}}$  in NSG mice. Blood (5  $\mu\text{l}$ ) was taken *via* tail bleeding at 2 min, 5 min, 10 min, 30 min, 1 h, 4 h and 24 h following intravenous injection of exosomes. **(B)** Excretion profile of  $[^{111}\text{In}]\text{DTPA-Exo}_{\text{B16}}$  in NSG mice where urine and faeces were collected from the animals 24 h post-injection. For **(A)** and **(B)**, the values are plotted in comparison with that of C57BL/6 presented in **Fig. 5**. **(C)** Organ biodistribution of  $[^{111}\text{In}]\text{DTPA-Exo}_{\text{B16}}$  in NSG mice. Animals were culled at 1 h, 4 h and 24 h post-injection, perfused with saline and their organs were excised for analysis by gamma counting. Inset shows the zoomed-in tumour accumulation values for each group. **(D)** Comparison of organ biodistribution of  $[^{111}\text{In}]\text{DTPA-Exo}_{\text{B16}}$  in C57Bl/6 and NSG mice 24 h post-injection, where inset shows zoomed-in tumour accumulation values for each group. Values are normalised to organ weight and expressed as mean  $\pm$  SD, where  $n=3$  for each group. For **(C)** and **(D)**, statistical analyses were done on liver, spleen, kidneys and tumour ( $p^* < 0.05$ ,  $p^{**} < 0.01$ ,  $p^{***} < 0.001$ ).

## Discussion

As described earlier, exosomes are very similar to cells in terms of being a phospholipid bilayer system, having the same membrane topology as their parent cells and inherently containing biomolecules such as proteins and RNAs as their cargo [14]. Therefore, [ $^{111}\text{In}$ ]Trop was hypothesised to result in successful radiolabelling of exosomes. This approach did lead to successful radiolabelling of the exosomes as described earlier, but at a much lower efficiency compared to that observed in platelets of ~60-80% [42]. Assuming platelet size to be 1  $\mu\text{m}$  in diameter [59] and that of  $\text{Ex}_{\text{OB16}}$  is ~130 nm (**Table 1**), and that both are perfect spheres, the number of  $\text{Ex}_{\text{OB16}}$  used in this study to determine the radiolabelling efficiency ( $3 \times 10^{11}$  particles) accounts for a total surface area which is about double that of the platelets used in the above study ( $2.2 \times 10^9$  platelets). However, the volume of an  $\text{Ex}_{\text{OB16}}$  particle is ~45 times lower than that of a single platelet. Therefore, although [ $^{111}\text{In}$ ]Trop complexes were able to translocate efficiently into the exosomal lumen due to the large total surface area, their significantly lower volume suggests a much lower amount of biomolecules within the exosomal lumen for  $^{111}\text{In}^{3+}$  to exchange with as compared to that in the cytoplasm of platelets.  $^{111}\text{In}^{3+}$  translocated into the exosomal lumen probably largely still exists as [ $^{111}\text{In}$ ]Trop due to the lack of biomolecules for exchange and are well able to leave the exosomal lumen, forming an equilibrium in terms of its concentration within and outside the lumen, contributing to the low radiolabelling efficiency and stability. This is corroborated by the similar radioactivity detected in the tumours of mice injected with  $^{111}\text{In}$ - $\text{Ex}_{\text{OB16}}$  24 h post-injection and that of the mice injected with free [ $^{111}\text{In}$ ]Trop, suggesting that the unexchanged  $^{111}\text{In}^{3+}$  in the form of [ $^{111}\text{In}$ ]Trop leaked out from the exosomal lumen into the circulation and gradually accumulates in the tumour (**Fig. S4C & S4D**). Another possibility for the low serum stability observed with intraluminal-labelled exosomes is that the serum might be damaging the vesicles, thereby releasing the entrapped [ $^{111}\text{In}$ ]Trop. However, this possibility is ruled out as very good serum stability was observed with the membrane-labelled exosomes (**Fig. 3B**).

The membrane or surface radiolabelling approach has been employed in synthetic nanocarriers such as polymeric nanocapsules and liposomes, whereby strong radioisotope chelators such as DTPA is incorporated as an integral component of their

polymeric shell or membrane respectively during synthesis. This allows the nanocarriers to be radiolabelled when incubated with radioisotopes such as  $^{111}\text{In}^{3+}$ , with their radiolabelling efficiency and stability reported to be between 61.9-100% and 78.2-91.3% respectively [56, 57, 60]. This strategy of DTPA incorporation however is not possible on biomolecules such as exosomes, and so bifunctional chelators are used instead. Bifunctional chelators are molecules that consist of a strong chelating agent such as DTPA on one end, and a biologically-reactive functional group on the other end, usually amine-reactive groups such as NHS-ester or anhydride, or thiol-reactive groups such as maleimide [61]. One such bifunctional chelator, cyclic DTPA-dianhydride (hereon referred to as DTPA-anhydride) was successfully conjugated to human serum albumin in a simple and rapid reaction, which allows subsequent radiolabelling with  $^{111}\text{In}^{3+}$  and its biodistribution analysed quantitatively [62]. DTPA-anhydride has since been demonstrated to be successfully conjugated to other biomolecules such as fibrinogen [63] and antibodies [64-67] without losing their specificity and function, enabling quantitative analysis of their biodistribution. This same DTPA-anhydride, which is now commercially available, was adopted in this study where it was conjugated to EXOB<sub>16</sub>, and a 5-fold increase in both radiolabelling efficiency and stability was observed (**Fig. 3A & 3B**).

Radiolabelling stability of [ $^{111}\text{In}$ ]DTPA-EXOB<sub>16</sub> was similar to that reported in the studies above, and this was expected as DTPA is attached to exosomes *via* the same stable amide bond. The radiolabelling efficiency of [ $^{111}\text{In}$ ]DTPA-EXOB<sub>16</sub> however is lower than that reported for the other nanocarriers, and this could be due to a lower number of DTPA molecules conjugated to EXOB<sub>16</sub>. In principle, this could be overcome by increasing the molar ratio of DTPA-anhydride in the reaction with the exosomes. However this would pose a problem due to rendering the reaction mixture more acidic due to the increasing amount of free DTPA forming from spontaneous hydrolysis in aqueous solution [67]. Given that the pK<sub>a</sub> of the side-chain amine on a lysine residue is ~10.5, low pH conditions would easily increase the proportion of the protonated form of the free amines of the lysine residues on the exosomal surface, making them weaker nucleophiles and thereby reducing the efficiency of the reaction [67]. This low pH could also adversely affect the function and integrity of other exosomal transmembrane proteins, which could affect the biodistribution as they have been reported to play a role in cell uptake [68-70]. This is

corroborated by studies that reported antibodies reacted with a high ratio of DTPA-anhydride had reduced antigen binding ability [64, 67]. It is therefore important to determine the number of free amines on exosomal surface prior to the reaction with DTPA. This is challenging due to the heterogeneity of exosomes, even the ones isolated from the same source. In this study, the number of free amines i.e. lysine residues on exosomes was assumed to be similar to that of bovine serum albumin (BSA) and this was used as the basis for reaction with DTPA-anhydride. In our hands, reactions using 1:80, 1:200, 1:400 and 1:800 (Lys:anhydride) molar ratios showed increasing radiolabelling efficiency with increasing molar ratio up to 1:400 (data not shown) after which a decline was observed. The molar ratio 1:400 was therefore chosen for the DTPA-Exo<sub>B16</sub> conjugation in this study.

Contaminating proteins from serum used in culture such as albumin and present in the Exo<sub>B16</sub> sample [47], are likely to compete with the exosomes for the reaction with DTPA-anhydride [62], thus lowering Exo<sub>B16</sub> labelling efficiency. Purifying exosome samples by gel filtration (e.g. Sepharose® CL-2B used in this study) or centrifugal filters (e.g. Nanosep®) prior to the labelling reaction can significantly reduce the amount of contaminating proteins in the sample, but this results in substantial loss of ~50% exosomes post-purification (**Fig. S7A and Fig. S7B**). This can pose a serious challenge when working with a limited number of exosomes either obtained from cell cultures or liquid biopsies. Gel filtration using Sepharose® CL-2B resin as the resolving matrix was chosen in this study due to its superior contaminating protein removal performance and thus significantly better improvement in the P:P ratio of the exosome sample, without altering the size of the exosomes (**Fig. S7B, Fig. S7C and Fig. S7D**). Hence, in case that radiolabelled proteins were formed, they could be efficiently removed along with excess unreacted DTPA-anhydride post-labelling. The radiolabelling efficiency of [<sup>111</sup>In]DTPA-Exo<sub>B16</sub> achieved in this study (**Fig. 3A**) was compliant to the “As Low As Reasonably Practicable” (ALARP) principle outlined by the UK’s Health and Safety Executive (HSE) in terms of radioactivity required to perform SPECT/CT imaging and quantitative biodistribution studies.

“As mentioned earlier, exosomal surface proteins play an important role in their interaction and subsequent uptake into cells, and that the disruption of these proteins can

influence their tissue uptake/localisation *in vitro* and *in vivo* [68, 70, 71]. DTPA-anhydride conjugation to exosomal surface proteins in the membrane labelling approach harbours such risk and could potentially influence the organ biodistribution of Exo<sub>B16</sub>. A dot blot analysis was carried out on the exosomes following a mock-radiolabelling protocol. It was found that surface proteins such as CD63 and CD9 are still present on the exosomes post-labelling, but showed a lower signal intensity upon detection (**Fig. S8**). This is most probably due to the conjugated DTPA causing slight hindering of the antibody binding. Further studies have to be carried out to investigate whether this would influence exosome uptake and accumulation in tissues *in vivo*.”

In this study, Exo<sub>B16</sub> showed rapid clearance from the circulation, accumulating predominantly in the liver and spleen. This accumulation profile is consistent with a number of other exosome biodistribution studies involving optical and nuclear modalities, where usually kidneys were reported to show the 3<sup>rd</sup> highest accumulation after the liver and spleen [18, 31-33, 72]. Other types of nanocarriers bearing physicochemical resemblance to exosomes such as liposomes and polymeric nanocapsules were also reported to accumulate mostly in the liver and spleen [56, 57, 60], which further supports the findings of this study. Lung accumulation is more commonly observed for non-spherical carbon-based nanocarriers with high aspect ratio or surface area such as carbon nanotubes and graphene [58, 73], but a number of studies using melanoma-derived exosomes however reported substantial exosome in the lungs. In two of these studies, B16-BL6 exosomes (murine melanoma) were engineered to express *Gaussia* luciferase (GL exosomes) and streptavidin (SAV-LA exosomes) respectively, showed prominent accumulation in liver and lungs [37, 39]. One study demonstrated that a high dose of exosomes administered intravenously resulted in asphyxia as a result of the exosome accumulation in the lungs [18]. However, the exosome dose administered in the former two studies (4-5 µg) were much lower than that of the latter (400 µg). Streptavidin was reported to naturally form tetramers in physiological conditions [74], and so the SAV-LA exosomes in the study could have formed aggregates from the interaction between the streptavidin molecules and accumulated in the lungs. However, the authors reported no size differences between the SAV-LA exosomes and unmodified ones from NTA analysis [39]. Size analysis however was not performed on the GL exosomes [37].

Another study, also using B16BL6 exosomes showed substantial lung accumulation, which was significantly reduced following the disruption of their exosomal surface proteins [71]. The surface protein disruption done in this study was by Proteinase K treatment for 30 minutes, which resulted in major ablation of surface proteins on B16BL6 exosomes, compared to the milder disruption on the surface proteins of Exo<sub>B16</sub> by DTPA incorporation in this study as discussed above. Therefore, the minimal lung accumulation of Exo<sub>B16</sub> observed in this study could not be attributed to the altered surface proteins. Although both B16BL6 and B16F10 are both melanoma-derived cell lines, the lung metastatic organotropism of the former was reported to be higher than that of the latter [75], thus it is likely that B16BL6 exosomes do home to the lungs to a greater extent than B16F10 exosomes. This is highlighted by a study that demonstrated exosomes derived from cancer cell lines with higher lung metastatic organotropism accumulated in lung tissues 3 times higher than those derived from cell lines with other metastatic organotropisms such as liver, bone and brain [76]. Another study showed B16F10 exosomes presence in lungs and bone marrow following intravenous administration, and that they induce greater metastasis of B16F10 cells to these sites compared to untreated controls [77]. However, the amount of exosomes present in these tissues were not properly quantified. To complicate the position further, exosome doses administered in these studies were expressed differently (i.e. in terms of particle number or  $\mu\text{g}$  protein), which does not allow direct comparison to the results in this work. This implies that the exosome doses administered in these studies may vary and was reported to also influence their biodistribution [32].

Another study by Lai et al. using exosomes from HEK293 cells showed a completely different exosome biodistribution profile to the one presented in this work. HEK293-derived exosomes accumulated to the greatest extent in the kidneys, followed by the liver, lungs and spleen [38]. The HEK293 exosomes had their surface engineered to have fusion protein constructs consisting of a PDGF-transmembrane domain for anchoring on the exosomal membrane; a biotin acceptor peptide sequence (BAP) for biotinylation by an exogenously expressed bacterial biotin ligase; and *Gaussia* luciferase. The modified exosomes here also did not show size differences from the unmodified exosomes [38]. Again, this study highlights the probable effect of introducing additional

moieties of relatively large size on exosomal membrane (e.g. luciferase and streptavidin) on the tissue tropism of exosomes *in vivo*, which concurs with the role of exosomal surface proteins on their tissue localisation discussed above. Substantial considerations are warranted when deciding on the modification status to be adapted for drug delivery applications, and it is therefore imperative that the biodistribution of engineered exosomes be compared with their unmodified counterparts to take into account any possible effect of the modification on their biodistribution. Thus, the membrane radiolabelling approach proposed in this work would serve as an excellent tool for this purpose.

Discrepancies between exosome biodistribution reported in the above studies including the results in this work could also be due to the different labelling and imaging modalities used. Previous work from our group [57, 78] demonstrated the difference between the biodistribution of the PLGA nanocapsules labelled with DiR or radiolabelled with <sup>111</sup>Indium, where nanocapsules labelled with DiR showed significantly higher lung accumulation as compared to the same nanocapsules which were radiolabelled by including 5-10% PLGA-PEG-DTPA in the excipients during formulation (i.e. without post-synthesis surface modification as done in this current work). Live whole body SPECT/CT imaging showed that the radiolabelled nanocapsules had a substantial lung accumulation at 1 h post-injection, which then continued to decrease over time from 4 h to 24 h, and this was supported by the quantitative organ biodistribution values obtained by gamma counting. Given the non-specific dye exchange phenomenon between membranes associated with lipophilic dyes such as DiR and PKH67 described earlier, the lung accumulation of DiR-labelled nanocapsules observed after 24 h is likely to come from the dye exchanged from the labelled nanocapsules to lung tissue where they initially accumulated in the early timepoint before redistributing to other organs, and this exchanged dye probably accumulated in the lungs over time up to 24 h. This highlights the robustness and reliability of using the nuclear modality in assessing exosome biodistribution and is the main motivation in developing the novel exosome radiolabelling approaches described in this study.

There are reports on naive exosomes having the potential of adopting the homing properties of their parent cell *in vivo* [32] or home to self-tissue *in vitro* [70]. In another study, the Exo<sub>B16</sub> in similar B16F10-bearing C57Bl/6 mice were reported to show tumour

accumulation of ~3% total administered fluorescence [32]. A separate study using PC3 and MCF-7 exosomes also showed similar self-tissue accumulation of ~2% ID/gT [70]. In our hands, fluorescently-labelled B16F10 exosomes (**Scheme S2** – supplementary information) showed good uptake in both B16F10 cells and GL261 (murine glioma) cells *in vitro*, but significantly higher uptake was seen in the former (**Fig. S9**) which suggests the self-homing potential of B16F10 exosomes. However, in this study, EX<sub>B16</sub> showed very low accumulation in B16F10 tumours *in vivo*, of less than 1% ID/gT. This low tumour accumulation of naïve exosomes, has been attributed to the rapid clearance of exosomes from the circulation by resident macrophages in organs that form part of the reticuloendothelial system (RES). A study demonstrated that depleting macrophages in mice by liposomal clodronate prior to exosome administration significantly increased their circulation time [79]. A separate study showed that by blocking the Scavenger Receptor Class A family (SR-A), a recently identified uptake receptor for exosomes in macrophages, liver accumulation of exosomes was significantly reduced while their circulation time increased, which led to a 3-fold increase in tumour accumulation *in vivo* [33]. Exosomes expressing CD47, which inhibits phagocytosis by macrophages upon binding to their SIRP $\alpha$  surface protein, were reported to have prolonged circulation time and resulted in better tumour uptake and ablation *in vivo* [80]. Flow cytometry analysis on EX<sub>B16</sub> showed that CD47 is expressed very minimally on their surface (**Fig. S10**), which corroborated with the observed rapid clearance of EX<sub>B16</sub> from the circulation. Similar analysis done on exosomes derived from other cancer and non-cancer cell lines suggested that CD47 is not a common marker of exosomes, and that this should be taken into account when interpreting the circulation profile of exosomes (**Fig. S10**). This highlights the importance of the endowment of active targeting moieties such as expression of targeting ligands as fusion constructs on exosomal surface proteins [14, 30], as well as developing strategies to bypass the RES organs as described above for effective targeted *in vivo* delivery of exosomes to non-RES sites such as tumours.

Immunodeficient mouse strains of various degrees of immune system impairment are used in studies involving human-derived tumour models to improve the engraftment success in mice. To date, the most immunodeficient mouse strain described is the NOD-*scid* ILR2 $\gamma^{null}$  (NSG) mice, whereby the NOD-mutation renders their innate immune cells

(particularly macrophages and dendritic cells) defective; the *scid*-mutation results in absence of the adaptive immune cells (T- and B-cells) and complement system, and the complete null mutation of the IL2R gene results in the absence of NK-cells as well as global defective cytokine-dependent signalling [81, 82]. In this study, although the B16F10 cells used to develop the subcutaneous tumour is of murine origin and therefore does not require an immunodeficient background for the host, NSG mice were chosen to serve as the extreme counterpart of the immunocompetent C57Bl/6 mice to investigate the influence of the immune system in Exo<sub>B16</sub> biodistribution. In this study, Exo<sub>B16</sub> biodistribution did not differ significantly between the C57Bl/6 and the NSG mice. However, looking at the kinetics of Exo<sub>B16</sub> accumulation in the RES organs of the NSG mice, the spleen initially recorded a lower signal, which increased by 3-fold between 4 h and 24 h to match that of the of the C57Bl6 mice (**Fig. 6C**). This delayed exosome accumulation in RES organs in immunodeficient mice was consistent with a study using NOD.CB17-Prkdcscid/J mice, and was attributed to the defective complement activation in opsonisation and therefore less effective uptake by phagocytic cells in mice with NOD-mutation background [18].

Interestingly, tumours of the immunocompetent mice showed significantly higher accumulation of Exo<sub>B16</sub> than that of the immunodeficient mice (**Fig. 6D**). Given the difference in the immune background of both mice strains, it is hypothesised that the difference in tumour accumulation values is due to the difference in the proportion of tumour-associated macrophages (TAMs) present in the tumours. Flow cytometry analysis on the total cells isolated from subcutaneous B16F10 tumours (gating strategy is described in supplementary information and **Fig. S11A**) developed in both strains of mice showed that tumours from the immunodeficient NSG mice had a significantly smaller population of TAMs (CD45<sup>+</sup> F4/80<sup>+</sup> CD11b<sup>+</sup>) (**Fig. S11b**) compared to that of the tumours from C57Bl/6 mice, which supports the hypothesis above. This suggests that tumour accumulation of exosomes in an immunodeficient host can be an underestimation compared to the actual value in an immunocompetent background. Therefore, it is important to relate the degree of immunity impairment of the animal model used to the results obtained for a more contextual interpretation of the data which might affect factors such as dosing for future therapy studies.

## Conclusions

The results in this work demonstrated that melanoma-derived exosomes were successfully and stably radiolabelled using a novel membrane radiolabelling approach. This has enabled a quantitative analysis of their biodistribution to be carried out in melanoma-bearing immunocompetent mice, showing high accumulation in the liver and spleen from the early time points up to 24 h, with marginal tumour (i.e. self-tissue) accumulation. This membrane radiolabelling approach also enabled a quantitative biodistribution comparison of the same exosomes in a similar tumour model but established in immunodeficient mice and showed that defective immune system did not influence the exosome biodistribution *in vivo* with the exception of the degree of their accumulation in the tumours. This novel membrane radiolabelling method is therefore a simple, reliable and more importantly, has the potential of radiolabelling any type of exosomes, isolated from either primary or immortalised cell cultures, and even from physiological fluids without requiring any **engineering** on the exosomes. It is hoped that this work will serve as an impetus in achieving a more standardised approach to understanding the *in vivo* fate of the many different types of exosomes thus rendering these future studies more comparable given the heterogeneous nature of exosomes. **Given the marginal self-tissue accumulation as opposed to the high RES-organ accumulation of naïve exosomes observed in this study, active targeting moieties appears to be essential to be imparted on exosomes for them to have a better prospect as an effective drug delivery system. Nonetheless, the *in vivo* biodistribution of naïve exosomes should always be studied and compared to that of their engineered counterpart, and this work provides an excellent tool for such comparative studies to be done reliably and accurately.**

## **Acknowledgements**

F. N. Faruqu is funded by the Malaysian government agency Majlis Amanah Rakyat (MARA). L. Xu is a recipient of the K.C. Wong Postdoctoral Fellowship and subsequently is a holder of the Marie Skłodowska-Curie Individual Fellowships (Horizon 2020) (H2020-MSCA-IF-2016). K. T. Al-Jamal acknowledges partial funding from the British Council (Newton Fund, 337313), BBSRC (BB/J008656/1) and Wellcome Trust (WT103913). The authors would also like to thank K.C. Mei for the useful scientific discussions on the radiolabelling method.

## References

1. Zitvogel L, Regnault A, Lozier A, Wolfers J, Flament C, Tenza D, et al. Eradication of established murine tumors using a novel cell-free vaccine: dendritic cell derived exosomes. *Nat Med*. 1998; 4: 594-600.
2. Raffai R, Li K, Wong D, Hong J. Therapeutic control of systemic inflammation & atherosclerosis with ApoE-polarized macrophage exosomes. *Atherosclerosis*. 2017; 263: e5-e6.
3. Masamune A, Yoshida N, Hamada S, Takikawa T, Nabeshima T, Shimosegawa T. Exosomes derived from pancreatic cancer cells induce activation and profibrogenic activities in pancreatic stellate cells. *Biochem Biophys Res Commun*. 2018; 495: 71-77.
4. Gangoda L, Liem M, Ang CS, Keerthikumar S, Adda CG, Parker BS, et al. Proteomic profiling of exosomes secreted by breast cancer cells with varying metastatic potential. *Proteomics*. 2017; 17: 1600370.
5. Wozniak M, Peczek L, Czernek L, Döchler M. Analysis of the mirna profiles of melanoma exosomes derived under normoxic and hypoxic culture conditions. *Anticancer Res*. 2017; 37: 6779-6789.
6. Salimu J, Webber J, Gurney M, Al-Taei S, Clayton A, Tabi Z. Dominant immunosuppression of dendritic cell function by prostate-cancer-derived exosomes. *J Extracell Vesicles*. 2017; 6: 1368823.
7. Lankford KL, Arroyo EJ, Nazimek K, Bryniarski K, Askenase PW, Kocsis JD. Intravenously delivered mesenchymal stem cell-derived exosomes target M2-type macrophages in the injured spinal cord. *PLoS One*. 2018; 13: e0190358.
8. Khalyfa A, Youssefnia N, Foster GE, Beaudin AE, Qiao Z, Pialoux V, et al. Plasma exosomes and improvements in endothelial function by angiotensin 2 type 1 receptor or cyclooxygenase 2 blockade following intermittent hypoxia. *Front Neurol*. 2017; 8: 709.
9. Manek R, Moghieb A, Yang Z, Kumar D, Kobessiy F, Sarkis GA, et al. Protein biomarkers and neuroproteomics characterization of microvesicles/exosomes from human cerebrospinal fluid following traumatic brain injury. *Mol Neurobiol*. 2018; 55: 6112-6128.
10. Pathare G, Dhayat NA, Mohebbi N, Wagner CA, Bobulescu IA, Moe OW, et al. Changes in V-ATPase subunits of human urinary exosomes reflect the renal response to acute acid/alkali loading and the defects in distal renal tubular acidosis. *Kidney Int*. 2018; 93: 871-880.
11. Liao Y, Du X, Li J, Lonnerdal B. Human milk exosomes and their microRNAs survive digestion in vitro and are taken up by human intestinal cells. *Mol Nutr Food Res*. 2017; 61: 1700082.
12. Kim J, Hong S-W, Kim S, Kim D, Hur D, Jin D-H, et al. Cyclooxygenase-2 expression is induced by celecoxib treatment in lung cancer cells and is transferred to neighbor cells via exosomes. *Int J Oncol*. 2017; 52: 613-620.
13. Sterzenbach U, Putz U, Low L-H, Silke J, Tan S-S, Howitt J. Engineered exosomes as vehicles for biologically active proteins. *Mol Ther*. 2018; 25: 1269-1278.
14. El Andaloussi S, Lakhali S, Mäger I, Wood MJA. Exosomes for targeted siRNA delivery across biological barriers. *Adv Drug Deliv Rev*. 2013; 65: 391-397.

15. Simhadri VR, Reiners KS, Hansen HP, Topolar D, Simhadri VL, Nohroudi K, et al. Dendritic cells release HLA-B-associated transcript-3 positive exosomes to regulate natural killer function. *PLoS One*. 2008; 3: e3377.
16. Santos JC, Lima NdS, Sarian LO, Matheu A, Ribeiro ML, Derchain SFM. Exosome-mediated breast cancer chemoresistance via miR-155 transfer. *Sci Rep*. 2018; 8: 829.
17. Hadla M, Palazzolo S, Corona G, Caligiuri I, Canzonieri V, Toffoli G, et al. Exosomes increase the therapeutic index of doxorubicin in breast and ovarian cancer mouse models. *Nanomedicine (Lond)*. 2016; 11: 2431-2441.
18. Smyth T, Kullberg M, Malik N, Smith-Jones P, Graner MW, Anchordoquy TJ. Biodistribution and delivery efficiency of unmodified tumor-derived exosomes. *J Control Release*. 2015; 199: 145-155.
19. Tian Y, Li S, Song J, Ji T, Zhu M, Anderson GJ, et al. A doxorubicin delivery platform using engineered natural membrane vesicle exosomes for targeted tumor therapy. *Biomaterials*. 2014; 35: 2383-2390.
20. Kim MS, Haney MJ, Zhao Y, Yuan D, Deygen I, Klyachko NL, et al. Engineering macrophage-derived exosomes for targeted paclitaxel delivery to pulmonary metastases: in vitro and in vivo evaluations. *Nanomedicine*. 2018; 14: 195-204.
21. Bellavia D, Raimondo S, Calabrese G, Forte S, Cristaldi M, Patinella A, et al. Interleukin 3- receptor targeted exosomes inhibit in vitro and in vivo chronic myelogenous leukemia cell growth. *Theranostics*. 2017; 7: 1333-1345.
22. Sun D, Zhuang X, Xiang X, Liu Y, Zhang S, Liu C, et al. A novel nanoparticle drug delivery system: The anti-inflammatory activity of curcumin is enhanced when encapsulated in exosomes. *Mol Ther*. 2010; 18: 1606-1614.
23. Tian T, Zhang HX, He CP, Fan S, Zhu YL, Qi C, et al. Surface functionalized exosomes as targeted drug delivery vehicles for cerebral ischemia therapy. *Biomaterials*. 2018; 150: 137-149.
24. Zhuang X, Xiang X, Grizzle W, Sun D, Zhang S, Axtell RC, et al. Treatment of brain inflammatory diseases by delivering exosome encapsulated anti-inflammatory drugs from the nasal region to the brain. *Mol Ther*. 2011; 19: 1769-1779.
25. Iessi E, Logozzi M, Lugini L, Azzarito T, Federici C, Spugnini EP, et al. Acridine orange/exosomes increase the delivery and the effectiveness of acridine orange in human melanoma cells: a new prototype for theranostics of tumors. *J Enzyme Inhib Med Chem*. 2017; 32: 648-657.
26. Aqil F, Jeyabalan J, Agrawal AK, Kyakulaga A-H, Munagala R, Parker L, et al. Exosomal delivery of berry anthocyanidins for the management of ovarian cancer. *Food Funct*. 2017; 8: 4100-4107.
27. Shtam TA, Kovalev RA, Varfolomeeva EY, Makarov EM, Kil YV, Filatov MV. Exosomes are natural carriers of exogenous siRNA to human cells in vitro. *Cell Commun Signal*. 2013; 11: 88.
28. Wahlgren J, Karlson TDL, Brisslert M, Vaziri Sani F, Telemo E, Sunnerhagen P, et al. Plasma exosomes can deliver exogenous short interfering RNA to monocytes and lymphocytes. *Nucleic Acids Res*. 2012; 40: e130.
29. Yang J, Zhang X, Chen X, Wang L, Yang G. Exosome mediated delivery of miR-124 promotes neurogenesis after ischemia. *Mol Ther Nucleic Acids*. 2017; 7: 278-287.

30. Alvarez-Erviti L, Seow Y, Yin H, Betts C, Lakhal S, Wood MJ. Delivery of siRNA to the mouse brain by systemic injection of targeted exosomes. *Nat Biotechnol.* 2011; 29: 341-345.
31. Ohno SI, Takanashi M, Sudo K, Ueda S, Ishikawa A, Matsuyama N, et al. Systemically injected exosomes targeted to EGFR deliver antitumor microRNA to breast cancer cells. *Mol Ther.* 2013; 21: 185-191.
32. Wiklander OP, Nordin JZ, O'Loughlin A, Gustafsson Y, Corso G, Mager I, et al. Extracellular vesicle in vivo biodistribution is determined by cell source, route of administration and targeting. *J Extracell Vesicles.* 2015; 4: 26316.
33. Watson DC, Bayik D, Srivatsan A, Bergamaschi C, Valentin A, Niu G, et al. Efficient production and enhanced tumor delivery of engineered extracellular vesicles. *Biomaterials.* 2016; 105: 195-205.
34. Progatky F, Dallman MJ, Lo Celso C. From seeing to believing: labelling strategies for in vivo cell-tracking experiments. *Interface Focus.* 2013; 3: 20130001.
35. Lehmann TP, Juzwa W, Filipiak K, Sujka-Kordowska P, Zabel M, Głowacki J, et al. Quantification of the asymmetric migration of the lipophilic dyes, DiO and DiD, in homotypic co-cultures of chondrosarcoma SW-1353 cells. *Mol Med Rep.* 2016; 14: 4529-4536.
36. Lassailly F, Griessinger E, Bonnet D. "Microenvironmental contaminations" induced by fluorescent lipophilic dyes used for noninvasive in vitro and in vivo cell tracking. *Blood.* 2010; 115: 5347-5354.
37. Takahashi Y, Nishikawa M, Shinotsuka H, Matsui Y, Ohara S, Imai T, et al. Visualization and in vivo tracking of the exosomes of murine melanoma B16-BL6 cells in mice after intravenous injection. *J Biotechnol.* 2013; 165: 77-84.
38. Lai CP, Mardini O, Ericsson M, Prabhakar S, Maguire CA, Chen JW, et al. Dynamic biodistribution of extracellular vesicles in vivo using a multimodal imaging reporter. *ACS Nano.* 2014; 8: 483-494.
39. Morishita M, Takahashi Y, Nishikawa M, Sano K, Kato K, Yamashita T, et al. Quantitative analysis of tissue distribution of the B16BL6-derived exosomes using a streptavidin-lactadherin fusion protein and iodine-125-labeled biotin derivative after intravenous injection in mice. *J Pharm Sci.* 2015; 104: 705-713.
40. Hwang DW, Choi H, Jang SC, Yoo MY, Park JY, Choi NE, et al. Noninvasive imaging of radiolabeled exosome-mimetic nanovesicle using 99m Tc-HMPAO. *Sci Rep.* 2015; 5: 15636.
41. Lynch S, Santos SG, Campbell EC, Nimmo AM, Botting C, Prescott A, et al. Novel MHC class I structures on exosomes. *J Immunol.* 2009; 183: 1884-1891.
42. Dewanjee MK, Rao SA, Didisheim P. Indium-111 tropolone, a new high-affinity platelet label: preparation and evaluation of labeling parameters. *J Nucl Med.* 1981; 22: 981-987.
43. Dewanjee M, Rao S, Rosemark J, Chowdhury S, Didisheim P. Indium-111 tropolone, a new tracer for platelet labeling. *Radiology.* 1982; 145: 149-153.
44. Signore A, Sensi M, Pozzilli C, Negri M, Lenzi G, Pozzilli P. Effect of unlabeled indium oxine and indium tropolone on the function of isolated human lymphocytes. *J Nucl Med.* 1985; 26: 612-615.
45. Goedemans WT. Simplified cell labelling with indium-111 acetylacetonate and indium-111 oxinate. *Br J Radiol.* 1981; 54: 636-637.

46. Thery C, Amigorena S, Raposo G, Clayton A. Isolation and characterization of exosomes from cell culture supernatants and biological fluids. *Curr Protoc Cell Biol.* 2006; 30: 3.22.21-23.22.29.
47. Webber J, Clayton A. How pure are your vesicles? *J Extracell Vesicles.* 2013; 2: 19861.
48. Théry C, Amigorena S, Raposo G, Clayton A. Isolation and Characterization of Exosomes from Cell Culture Supernatants. *Current protocols in cell biology.* 2006; 3: 1-29.
49. Thakur ML, McKenney S. Techniques of Cell Labeling: An Overview. In: Thakur ML, Ezikowitz MD, Hardeman MR, editors. *Radiolabeled Cellular Blood Elements.* Boston, MA: Springer US; 1985. p. 67-87.
50. Bandyopadhyay D, Schiff RG, Hoory S, Moskowitz GW, Levy LM, Das DK. <sup>111</sup>Indium-tropolone labeled human PMNs: a rapid method of preparation and evaluation of labeling parameters. *Inflammation.* 1987; 11: 13-22.
51. Danpure HJ, Osman S. Optimum conditions for radiolabelling human granulocytes and mixed leucocytes with <sup>111</sup>In-tropolonate. *Eur J Nucl Med.* 1988; 13: 537-542.
52. Bindslev L, Haack-Sørensen M, Bisgaard K, Kragh L, Mortensen S, Hesse B, et al. Labelling of human mesenchymal stem cells with indium-111 for SPECT imaging: effect on cell proliferation and differentiation. *Eur J Nucl Med Mol Imaging.* 2006; 33: 1171-1177.
53. Welling M, Duijvestein M, Signore A, van der Weerd L. In vivo biodistribution of stem cells using molecular nuclear medicine imaging. *J Cell Physiol.* 2011; 226: 1444-1452.
54. Beliard A, Noël A, Goffin F, Frankenne F, Foidart J-M. Adhesion of endometrial cells labeled with <sup>111</sup>Indium-tropolonate to peritoneum: a novel in vitro model to study endometriosis. *Fertil Steril.* 2003; 79: 724-729.
55. Laan AC, Santini C, Jennings L, de Jong M, Bernsen MR, Denkova AG. Radiolabeling polymeric micelles for in vivo evaluation: a novel, fast, and facile method. *EJNMMI Res.* 2016; 6: 12.
56. Hodgins NO, Wang JT-W, Klippstein R, Costa PM, Sosabowski JK, Marshall JF, et al. Investigating in vitro and in vivo  $\alpha\beta 6$  integrin receptor-targeting liposomal alendronate for combinatory  $\gamma\delta$  T cell immunotherapy. *J Control Release.* 2017; 256: 141-152.
57. Bai J, Wang JTW, Rubio N, Protti A, Heidari H, Elgogary R, et al. Triple-modal imaging of magnetically-targeted nanocapsules in solid tumours in vivo. *Theranostics.* 2016; 6: 342-356.
58. Wang JTW, Fabbro C, Venturelli E, Ménard-Moyon C, Chaloin O, Da Ros T, et al. The relationship between the diameter of chemically-functionalized multi-walled carbon nanotubes and their organ biodistribution profiles in vivo. *Biomaterials.* 2014; 35: 9517-9528.
59. Wilkerson MJ, Shuman W, Swist S, Harkin K, Meinkoth J, Kocan AA. Platelet size, platelet surface-associated IgG, and reticulated platelets in dogs with immune-mediated thrombocytopenia. *Vet Clin Pathol.* 2001; 30: 141-149.
60. Hodgins NO, Wang JT, Parente-Pereira AC, Liu M, Maher J, Al-Jamal KT. In vitro potency, in vitro and in vivo efficacy of liposomal alendronate in combination with  $\gamma\delta$  T cell immunotherapy in mice. *J Control Release.* 2016; 241: 229-241.

61. Brechbiel MW. Bifunctional chelates for metal nuclides. *Q J Nucl Med Mol Imaging*. 2008; 52: 166-173.
62. Hnatowich D, Layne W, Childs R. The preparation and labeling of DTPA-coupled albumin. *Int J Appl Radiat Isot*. 1982; 33: 327-332.
63. Layne W, Hnatowich D, Doherty P, Childs R, Lanteigne D, Ansell J. Evaluation of the viability of In-111-labeled DTPA coupled to fibrinogen. *J Nucl Med*. 1982; 23: 627-630.
64. Hnatowich D, Layne W, Childs R, Lanteigne D, Davis M, Griffin TW, et al. Radioactive labeling of antibody: a simple and efficient method. *Science*. 1983; 220: 613-615.
65. Hnatowich D, Childs R, Lanteigne D, Najafi A. The preparation of DTPA-coupled antibodies radiolabeled with metallic radionuclides: an improved method. *J Immunol Methods*. 1983; 65: 147-157.
66. Kinsey BM, Macklis RM, Ferrara JM, Layne WW, Burakoff SJ, Kassis AI. Efficient conjugation of DTPA to an IgM monoclonal antibody in ascites fluid. *Int J Rad Appl Instrum B*. 1988; 15: 285-292.
67. Paik C, Ebbert M, Murphy P, Lassman C, Reba R, Eckelman W, et al. Factors influencing DTPA conjugation with antibodies by cyclic DTPA anhydride. *J Nucl Med*. 1983; 24: 1158-1163.
68. Escrevente C, Keller S, Altevogt P, Costa J. Interaction and uptake of exosomes by ovarian cancer cells. *BMC Cancer*. 2011; 11: 108.
69. Rana S, Yue S, Stadel D, Zöller M. Toward tailored exosomes: the exosomal tetraspanin web contributes to target cell selection. *Int J Biochem Cell Biol*. 2012; 44: 1574-1584.
70. Smyth TJ, Redzic JS, Graner MW, Anchordoquy TJ. Examination of the specificity of tumor cell derived exosomes with tumor cells in vitro. *Biochim Biophys Acta*. 2014; 1838: 2954-2965.
71. Charoenviriyakul C, Takahashi Y, Morishita M, Nishikawa M, Takakura Y. Role of extracellular vesicle surface proteins in the pharmacokinetics of extracellular vesicles. *Mol Pharm*. 2018; 15: 1073-1080.
72. Charoenviriyakul C, Takahashi Y, Morishita M, Matsumoto A, Nishikawa M, Takakura Y. Cell type-specific and common characteristics of exosomes derived from mouse cell lines: yield, physicochemical properties, and pharmacokinetics. *Eur J Pharm Sci*. 2017; 96: 316-322.
73. Liu J-H, Yang S-T, Wang H, Chang Y, Cao A, Liu Y. Effect of size and dose on the biodistribution of graphene oxide in mice. *Nanomedicine (Lond)*. 2012; 7: 1801-1812.
74. Hsu C-K, Park S. Computational and mutagenesis studies of the streptavidin native dimer interface. *J Mol Graph Model*. 2010; 29: 295-308.
75. Rondepierre F, Defay C, Bouchon B, Papon J, Arlotto M, Berger F, et al. Comparative studies of B16F10 and B16Bl6 protein profiles in cell culture and mouse serums. *Melanoma Res*. 2006; 16: S58-S59.
76. Hoshino A, Costa-Silva B, Shen T-L, Rodrigues G, Hashimoto A, Tesic Mark M, et al. Tumour exosome integrins determine organotropic metastasis. *Nature*. 2015; 527: 329-335.
77. Peinado H, Alečković M, Lavotshkin S, Matei I, Costa-Silva B, Moreno-Bueno G, et al. Melanoma exosomes educate bone marrow progenitor cells toward a pro-metastatic phenotype through MET. *Nat Med*. 2012; 18: 883-891.

78. Klippstein R, Wang JT-W, El-Gogary RI, Bai J, Mustafa F, Rubio N, et al. Passively targeted curcumin-loaded PEGylated PLGA nanocapsules for colon cancer therapy in vivo. *Small*. 2015; 11: 4704-4722.
79. Imai T, Takahashi Y, Nishikawa M, Kato K, Morishita M, Yamashita T, et al. Macrophage-dependent clearance of systemically administered B16BL6-derived exosomes from the blood circulation in mice. *J Extracell Vesicles*. 2015; 4: 26238.
80. Kamekar S, LeBleu VS, Sugimoto H, Yang S, Ruivo CF, Melo SA, et al. Exosomes facilitate therapeutic targeting of oncogenic KRAS in pancreatic cancer. *Nature*. 2017; 546: 498-503.
81. Shultz LD, Lyons BL, Burzenski LM, Gott B, Chen X, Chaleff S, et al. Human lymphoid and myeloid cell development in NOD/LtSz-scid IL2R $\gamma$  null mice engrafted with mobilized human hemopoietic stem cells. *J Immunol*. 2005; 174: 6477-6489.
82. Ishikawa F, Yasukawa M, Lyons B, Yoshida S, Miyamoto T, Yoshimoto G, et al. Development of functional human blood and immune systems in NOD/SCID/IL2 receptor  $\gamma$  chain null mice. *Blood*. 2005; 106: 1565-1573.